

Observation of disorder-induced superfluidity

Google Quantum AI and collaborators [†]

The emergence of states with long-range correlations in a disordered landscape is rare, as disorder typically suppresses the particle mobility required for long-range coherence. But when more than two energy levels are available per site, disorder can induce resonances that locally enhance mobility. Here we explore phases arising from the interplay between disorder, kinetic energy, and interactions on a superconducting processor with qutrit readout and control. Compressibility measurements distinguish an incompressible Mott insulator from surrounding compressible phases and reveal signatures of glassiness, reflected in non-ergodic behavior. Spatially-resolved two-point correlator measurements identify regions of the phase diagram with a non-vanishing condensate fraction. We also visualize the spectrum by measuring the dynamical structure factor. A linearly-dispersing phonon mode materializes in the superfluid, appearing even when disorder is introduced to the clean Mott insulator. Our results provide strong experimental evidence for disorder-induced superfluidity.

Condensate formation, as in superfluids or superconductors, necessitates the onset of long-range phase coherence. This coherence manifests as the macroscopic occupation of a single quantum state[1]. Such states are generally fragile to spatial inhomogeneities that relax momentum and reduce the condensate fraction; impurities or boundary effects will scramble the phase of a propagating particle, resulting in predominantly destructive interference between paths and driving the system into an insulating state. The localization of the many-body wavefunction is generally believed to be incompatible with extended phases of matter such as superfluidity. Nonetheless, in a multi-level bosonic system, disorder could lead to local condensate formation by enhancing resonant tunneling between nearby sites. These processes can give rise to rare-region effects, where atypical pockets of nearly resonant sites form local coherent puddles within a globally disordered system. Here, we show that these local mechanisms can give rise to a macroscopic superfluid characterized by long-range phase coherence and linearly-dispersing phonon modes.

In this work, we study the low-energy phase diagram of strongly interacting bosons on a two-dimensional lattice. Independent tuning of on-site disorder W and nearest-neighbor hopping J (Fig. 1) allows us to traverse the insulator–superfluid transition and probe distinct insulating phases. The interplay between these parameters has been extensively explored through analytical [2, 3], numerical [4–6], and experimental studies in both solid-state [7–9] and ultracold-atom platforms [10–16].

At low disorder and when the kinetic energy is much smaller than the interaction energy, $J/U \ll 1$, the system is in a strongly-correlated Mott insulator (MI) phase, characterized by a finite gap to single-particle excitations. As hopping between adjacent sites increases, the system undergoes a quantum phase transition to a superfluid (SF) phase, where bosons can move freely. At low hopping J , increasing disorder drives a transition from the MI to the Bose glass (BG) phase—a gapless insulator whose properties and boundaries remain under debate [3, 6, 17–20]. Superfluidity—flow without viscosity—is inherently a dynamical phenomenon. Thus, while long-

range phase coherence is a prerequisite for superfluidity, frequency-resolved probes are necessary for providing unambiguous evidence for the phase. Direct experimental detection of disorder-induced superfluidity has remained elusive, largely due to the difficulty of resolving dynamical quantities in quantum simulators or synthesizing materials with tunable disorder.

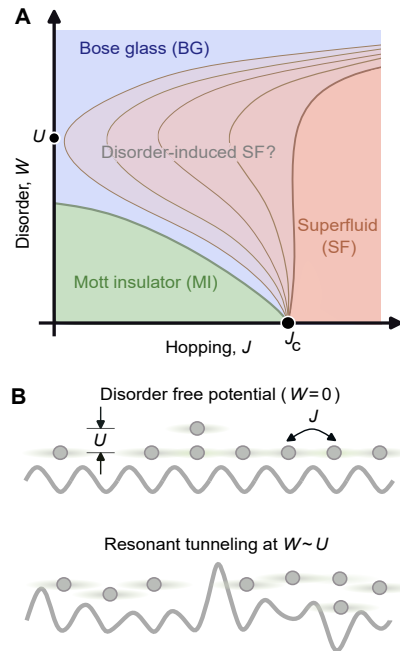


FIG. 1. **Phases of interacting bosons in a disordered landscape.** (A) Heuristic phase diagram as a function of hopping (J) and disorder strength (W), with U the on-site interaction. Theory and numerics [6, 18] point to a ‘re-entrant’ disorder-mediated superfluid phase above the Mott insulator; however, no evidence for this has been observed experimentally. (B) For $W = 0$, once J exceeds a critical value J_c , bosons hop freely between sites and form a coherent superfluid. Although disorder localizes single-particle states, particles may undergo short-range resonant tunneling—which could, in principle, promote superfluidity.

The transmon-based quantum processor used here

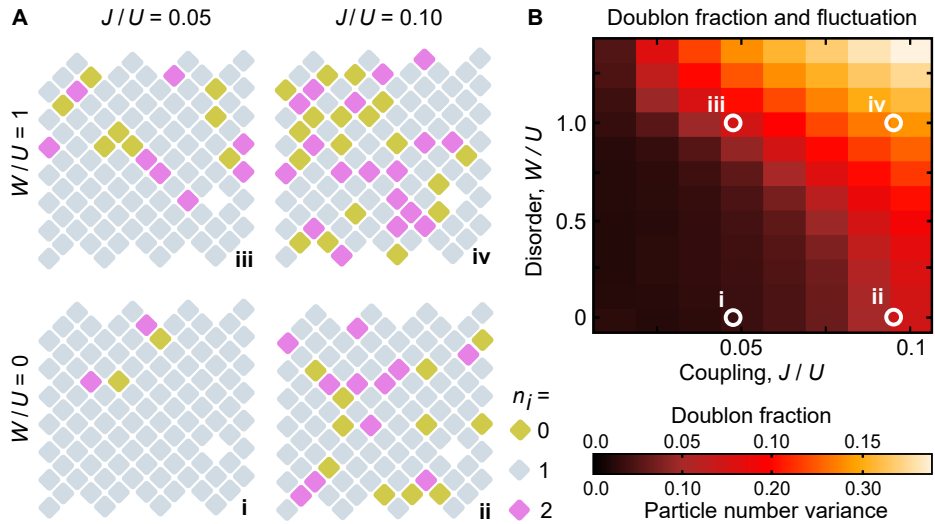


FIG. 2. **Formation of particle-hole excitations.** (A) Typical single-shot density measurements, showing doublon ($n_i = 2$) and holon ($n_i = 0$) formation at four different points in the J - W phase diagram using a 2D grid of qutrits at fixed interaction strength $U/(2\pi) = 190$ MHz. As J/U is increased, more particle-hole pairs are formed. Data is post-selected to enforce number conservation, yielding matched holon and doublon counts. (B) Measured doublon fraction in the J - W parameter plane, averaged over 10,000 measurement instances and 10 disorder realizations over a 4×9 grid of qutrits. Since $\langle n \rangle = 1$, the spatially averaged excitation number variance, $\langle n^2 \rangle - \langle n \rangle^2$, can be directly obtained by multiplying the measured doublon fraction by 2.

is assembled from a two-dimensional array of coupled nonlinear superconducting resonators. The elementary excitations—microwave photons in each resonator—obey Bose-Einstein statistics. Any integer number of microwave photons can, in principle, occupy the same resonator. The physics of these strongly interacting bosons can be effectively captured by the Bose-Hubbard model,

$$H = -J \sum_{\langle i,j \rangle} \left(a_i^\dagger a_j + a_j^\dagger a_i \right) + \frac{U}{2} \sum_i n_i (n_i - 1) - \sum_i \mu_i n_i, \quad (1)$$

where $a_i^\dagger = |1\rangle\langle 0| + \sqrt{2}|2\rangle\langle 1| + \dots$ describes a creation operator for a boson at site i . Hopping between nearest neighboring sites is mediated by tunable coupling elements [21] with coupling constant J ; $n_i \equiv a_i^\dagger a_i$ is the number operator at site i ; U is the on-site Hubbard repulsion; and the on-site potential, μ_i , is drawn from a uniform distribution centered at some fixed chemical potential μ with width W : $\mu_i \sim \mu + \text{Unif}[-W/2, W/2]$. By engineering the initial states and adiabatic protocols, we restrict the dynamics to a regime where at most two excitations reside on any given site (Fig. 2), effectively treating the resonators as ‘qutrits’. This occupancy constraint is enforced by the strength of the transmon nonlinearity.

The ground state phase diagram of this model was first characterized analytically by Fisher *et al.* [2] and later quantified numerically [4, 5]. In the clean two-dimensional (2D) system, a phase transition between the Mott insulator (MI) and superfluid (SF) is expected at $J_c/U \simeq 0.06$. The existence of a re-entrant superfluid ‘finger’ above small J , most prominent for values of $W \sim U$, has also been proposed on the basis of Monte-Carlo

data [6, 18]. Early studies of the disordered superfluid-to-insulator transition were performed on porous helium-4 films [7] and in granular superconductors. Both the clean [10] and disordered [14–16] Bose-Hubbard models have also been realized in optical lattices, and the essential characteristics, such as phase coherence in the superfluid and non-ergodicity in the Bose glass, have been reported [22–29]. The existence of a re-entrant superfluid phase mediated by disorder has been disputed, with most works [30] finding that increased disorder leads to increased dissipation and localization incompatible with superfluidity in one spatial dimension (1D) [17, 31], 2D [32, 33], and 3D [34, 35]. There are some indications, however, that repulsive interactions can promote delocalization and phase coherence [36]. To our knowledge, there exists no definitive experimental evidence of re-entrant disorder-induced superfluidity in the Bose-Hubbard model.

To visualize particle-hole formation, we initialize a 2D array of qutrits at commensurate unit filling, $n = 1$, by placing a single excitation on each site: $|111\dots\rangle$. To remain in the low-energy subspace, we adiabatically ramp to target Hamiltonian parameters (see Supp.). In Fig. 2 we show typical boson populations as a function of J and W . We observe an increased density of doublons (the $|2\rangle$ qutrit state), matched by holon formation (the $|0\rangle$ state) on other sites, with the total density of particle-hole excitations growing with the disorder strength W or coupling J (brighter colors in panel B). The increased doublon–holon incidence as a function of W can be understood as arising when detunings between nearby sites approach U and hence permit tunneling, making particle–hole pairs energetically favorable.

The particle-number fluctuation $\langle n^2 \rangle - \langle n \rangle^2$, exactly

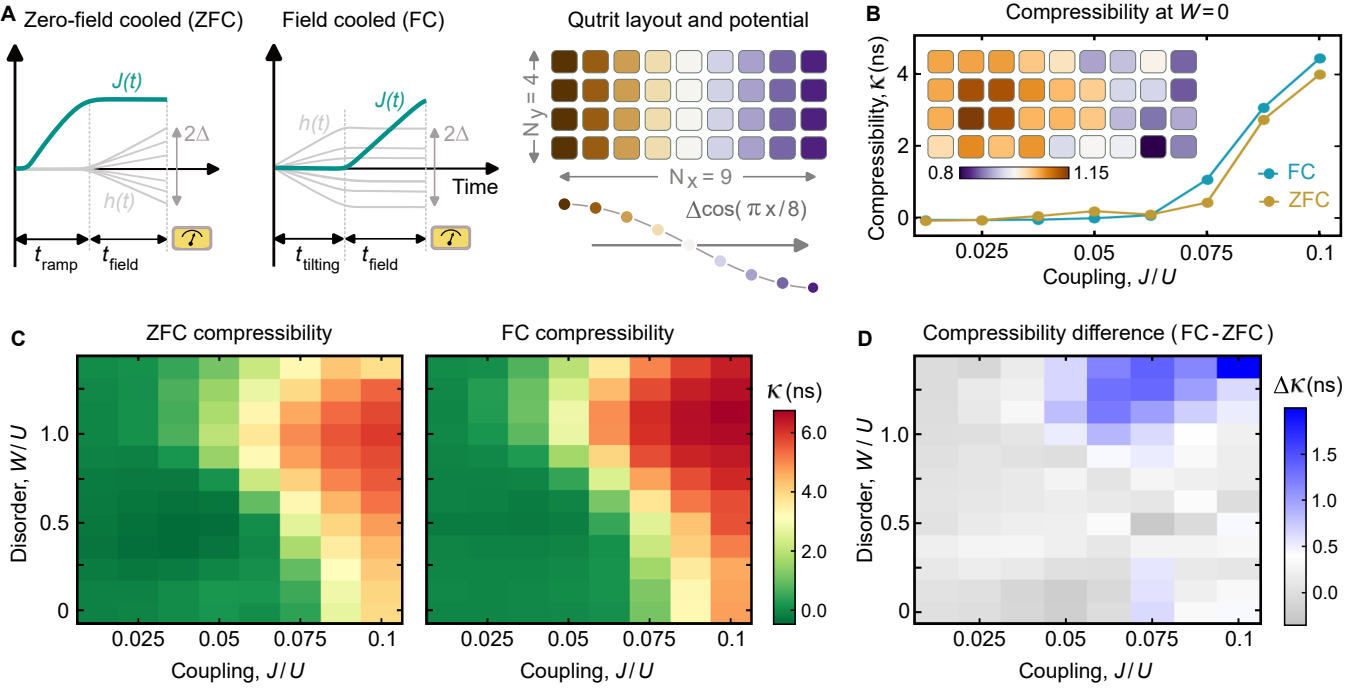


FIG. 3. **Mapping the compressibility in the $J - W$ plane** (A) Annealing ramp protocols, analogous to ‘field-cooling’ (FC) and ‘zero-field-cooling’ (ZFC) experiments in glasses. In the ZFC case, the potential gradient is applied after the state has been adiabatically prepared; for the FC ramps, the gradient is applied during state preparation, with $t_{\text{ramp}} = 100$ ns and $t_{\text{field}} = 250$ ns. In a $N_x = 9$ by $N_y = 4$ grid, the on-site potentials are ramped to $\Delta \cos(\pi x/8)$, with perturbation strength $\Delta/(2\pi) = 30$ MHz. (B) Compressibility as a function of J at zero disorder, measured using both the ZFC (brown) and FC (blue) protocols. The inset shows $\langle n_i \rangle$ at $J/U = 0.1$ and $W = 0$ for a state prepared with the FC protocol. (C) Compressibility in the $J-W$ plane, displaying transition to a compressible state as W and J are increased, measured using both the ZFC (left) and FC (right) protocols. 150 disorder realizations were taken. (D) Difference in compressibility, $\Delta\kappa$, between FC and ZFC protocols, revealing a non-ergodic corner of the phase diagram ($\Delta\kappa \neq 0$, shaded blue).

equal to twice the doublon fraction, can also be readily extracted from our measurements. This quantity, considered as a function of J and W , reflects the basic properties of the MI and SF phases: the MI phase has a finite gap to single-particle excitations, which remain well localized on individual lattice sites, whereas the SF phase is gapless and supports freely propagating excitations with well-defined momenta. This reasoning is commonly used to identify phases in cold-atom systems [10].

On-site particle-number fluctuations $\langle n_i^2 \rangle - \langle n_i \rangle^2$, as shown in Fig. 2B, may reflect either particle mobility or the underlying disordered potential landscape. As such, this metric is not an appropriate diagnostic for the compressibility in the presence of intermediate-to-strong disorder (see Supp. for further discussion). We instead quantify the compressibility κ by measuring the system’s response, $\langle \delta n_i \rangle$, to an applied potential gradient, $\delta\mu$. A non-zero compressibility, $\kappa \equiv (\partial n / \partial \mu) > 0$, indicates a finite density of excitations at zero energy, thus allowing us to distinguish the gapped MI from surrounding compressible phases. Crucially, in the presence of disorder, the observables might depend on the path taken through phase space during preparation of the Hamiltonian. If two different state preparation protocols (Fig. 3A) yield different values of the compressibility, $\kappa_{\text{path 1}} \neq \kappa_{\text{path 2}}$, then

the system is non-ergodic over experimentally-accessible timescales. This observation allows us to distinguish between non-ergodic glass-like states and surrounding ergodic states such as MI and SF. Accordingly, we implement two protocols: (1) prepare the state by first bringing qutrits to resonance and ramping up $J(t)$ before applying the gradient, or (2) apply the cosine perturbation first and then prepare the state—in the presence of the applied field—by ramping up $J(t)$. We refer to these as “zero-field cooled” (ZFC) and “field-cooled” (FC), respectively, in analogy to classical experiments on glassy systems [37].

To measure κ , a static perturbation $\mu_i \rightarrow \mu_i + \Delta \cos(\pi x_i/L)$ is applied to each of the on-site potentials, and the response is measured:

$$\kappa = \frac{2}{N\Delta} \sum_i \langle n_i \rangle \cos(\pi x_i/L). \quad (2)$$

In Fig. 3B, we plot the compressibility obtained using both the FC and ZFC protocols as a function of J when $W = 0$. In panel (C), we extend the measurements to the full $J - W$ plane, and observe that the onset of compressibility coincides with the emergence of particle-hole excitations as seen in Fig. 2. The incompressible phase (green area) is gapped; a finite amount of energy, of order

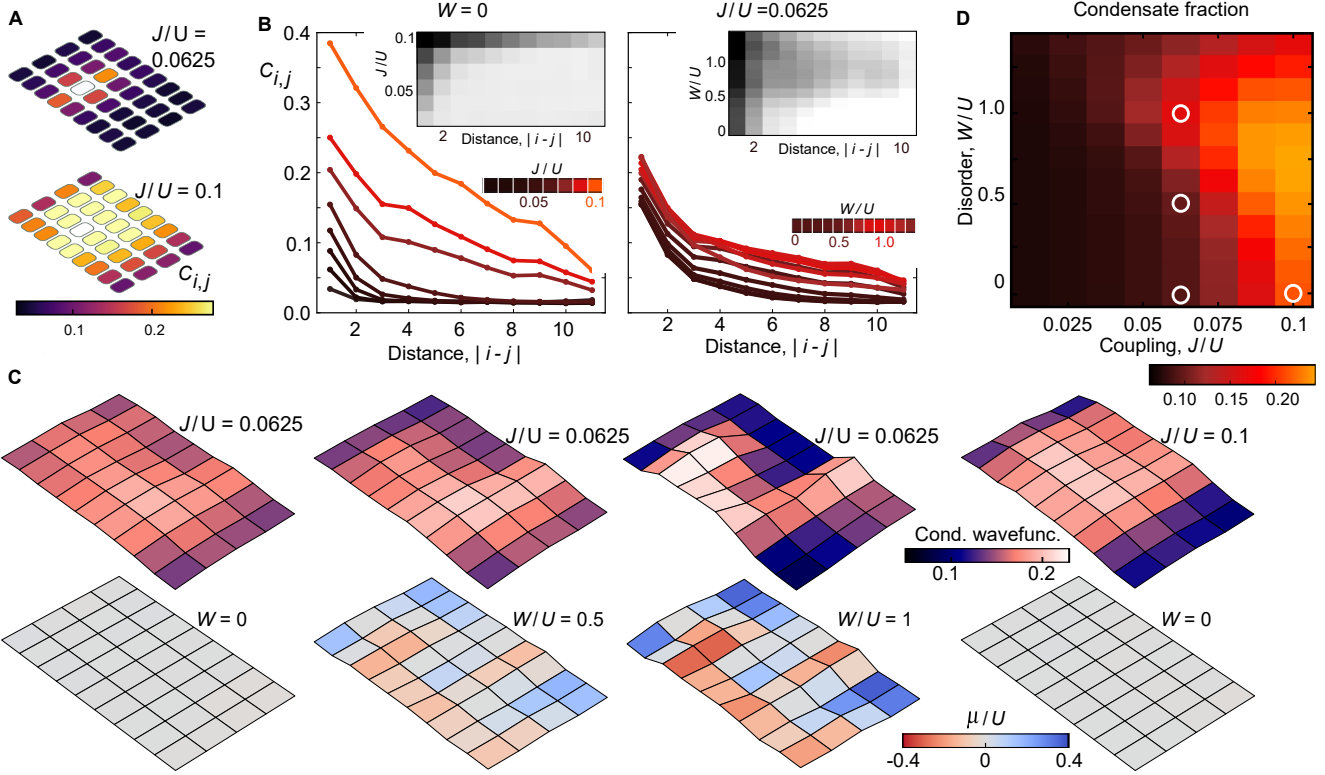


FIG. 4. **Characterizing the condensate** (A) C_{ij} is measured relative to a fixed qubit i for two values of J/U with zero disorder. The qubit grid has dimension 4×9 . (B) C_{ij} averaged over all pairs as a function of Manhattan distance, $|i-j|$. We take a cut at $W = 0$ (left) and $J = 0.0625U$ (right). For the latter measurement, 10 disorder realizations are taken. The insets show the same data in grayscale. (C) Condensate wavefunction for four different combinations of J and W . (D) The condensate fraction, extracted from the largest eigenvalue of C_{ij} , in the J - W plane. When $W \neq 0$, 10 disorder realizations are averaged.

U , is required to bridge the gap above the ground state. This gapped insulator can be identified as a Mott, i.e. ‘correlated’, insulator. While both protocols indicate the existence of a compressible state as a function of either increasing J or W , the reported value of the compressibility differs at large disorder (blue region in Fig. 3D). This difference is a hallmark of glassy behavior and possibly signals a breakdown of ergodicity [38], at least on the timescales accessible to this experiment. Note that κ is the static, long-wavelength limit of the dynamical structure factor, which we define and measure in Fig. 5.

A distinguishing property of superfluidity is the macroscopic occupation of a single quantum state, reflected in the emergence of a non-zero condensate fraction $n_0 \gg 1/N$ (N being the total number of particles). To obtain this quantity, we construct the spatially-resolved two-point correlator, defined

$$C_{ij} \equiv \langle a_i^\dagger a_j \rangle, \quad (3)$$

where C_{ij} is the single-particle density matrix (SPDM) whose largest eigenvalue, λ_0 , gives the condensate fraction $n_0 \equiv \lambda_0/N$ [39]. We interpret n_0 as the fraction of particles in the macroscopically occupied $k \rightarrow 0$ mode, serving as a proxy for phase coherence. In Fig. 4A we

show two typical instances of C_{ij} in a disorder-free landscape, fixing i to a given lattice site (marked in white) and showing its correlation with all other sites j . We plot results for $J/U = 0.0625$ (top), in the MI, and $J/U = 0.1$ (bottom), which is deep in the SF phase. The two-point correlator shows rapid spatial decay in the MI, whereas in the SF the correlations are stronger and decay more slowly. In Fig. 4B we measure C_{ij} for all i, j pairs and plot the correlator as a function of Manhattan distance for various values of J at $W = 0$ (left) and for a range of W values at fixed $J = 0.0625U$ (right). In the MI phase, the correlations decay rapidly to a constant background (left plot, dark lines), whereas C_{ij} becomes significantly longer-ranged as J approaches $0.1U$ (left plot, brighter colors). The cut at $J/U = 0.0625$ shows a non-monotonic dependence on disorder strength. As seen more clearly in the inset plots, C_{ij} develops longer-ranged behavior around $W \sim U$. This suggests that when the disorder is on the order of U , the generation of particle-hole pairs is promoted by resonances between sites with mutual detuning U ; this, in turn, can lead to the emergence of long-range phase coherence.

By measuring C_{ij} for all i, j pairs in a 4×9 lattice of qutrits, we construct the full SPDM. Its largest nor-

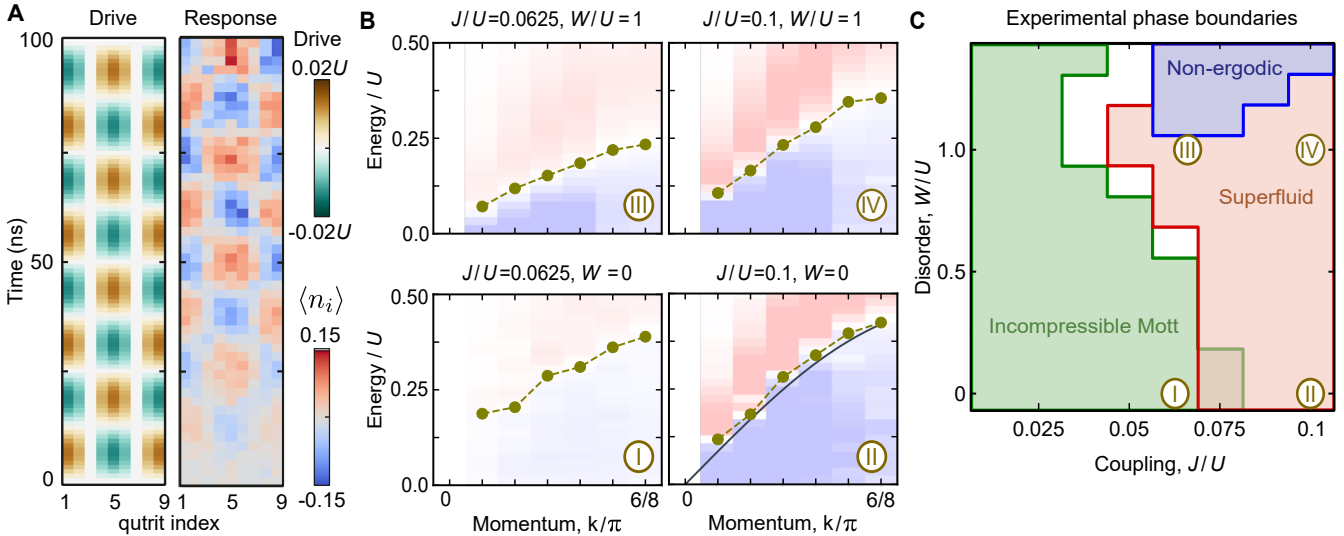


FIG. 5. **Direct measurement of dynamical structure factor.** (A) After preparing the desired state on a 4×9 grid of qubits, we apply a spatiotemporal potential modulation pattern and then measure $\langle n_i \rangle$ at each site (see Supp.). We show a typical drive (left) and response (right) with momentum $k = 2\pi/8$ and frequency $\omega/(2\pi) = 40$ MHz. The drive is spatially uniform over the shorter dimension and sinusoidal in the other dimension. The response shown here has subtracted from it the response with no drive and is averaged over the smaller spatial dimension. (B) Reactive part of the space- and time-resolved $\langle n \rangle$, after averaging over the shorter dimension ($L = 4$). 10 disorder realizations are taken for experiments where $W \neq 0$. The locations of the zeros (where the system is maximally absorptive, corresponding to its fundamental modes) are indicated by brown dots. Theory prediction using the Gutzwiller ansatz (see Supp.) is plotted in black for the disorder-free experiments. (C) Phase boundaries were identified by binarization of the compressibility, the difference between ZFC and FC (Fig. 3), and the condensation fraction measurements (Fig. 4). The 4 parameter points used in Fig. 5 B are shown with encircled numbers.

malized eigenvalue and corresponding eigenfunction yield the condensate fraction and condensate wavefunction, respectively. In Fig. 4C we show four example condensate wavefunctions, matched to the disorder landscapes that produced them in the bottom row. A clear correlation between the on-site disorder and the spatial variation of the wavefunction is observed. The condensation pattern at $J/U = 0.1$ in the disorder-free case (far right) resembles a standing wave, as expected. When $W \neq 0$, we find that the condensate wavefunction tracks the underlying disordered landscape. In (D) we summarize these data by plotting the condensation fraction, obtained from SPDM measurements, across the J - W plane. This plot confirms the signatures hinted at in other panels: the emergence of a condensate with increasing disorder, peaked for disorder strength close to the Hubbard U .

Superfluidity is distinguished by its dynamical and topological properties, including frictionless flow and the emergence of collective excitations. This contrasts with Bose-Einstein condensation, a ground-state phenomenon that can arise even in the absence of interactions. Among the most notable of these dynamical features is the emergence of sound—gapless, linearly-propagating Bogoliubov modes. While a direct measurement of the excitation spectrum is difficult, we can nevertheless probe the dynamical structure factor,

$$\chi^R(x_i, t; x_j, t') = -i\Theta(t - t')\langle [n(x_i, t), n(x_j, t')]\rangle, \quad (4)$$

where Θ is the Heaviside step function, by driving the

system with a standing wave in the horizontal direction at fixed wave-vector $k = \pi m/L$ and frequency ω (Fig. 5 A), $\mu_j \rightarrow \Delta \sin(\omega t) \cos(kx_j)$ with $L = 8$. In the condensate, the poles of the structure factor coincide with those of the phonon mode to all orders in perturbation theory. This surprising coincidence in the spectra derives from the condensate-induced intermixing of single-particle and density excitations [40]. The dynamical structure factor thus reveals a branch of the quasiparticle spectrum, offering complementary evidence for superfluidity beyond that captured by the condensate fraction.

In Fig. 5 B we plot the real part of the Fourier-transformed dynamical structure factor for different values of J and W . By locating the zero-crossing of the reactive response, we can extract the points in (k, ω) space that are most absorptive; in other words, the modes of the system. We observe very little response in the Mott insulator (I). By contrast, the superfluid exhibits a linearly-dispersing mode, as shown in (II). At weak hopping and near-critical disorder, i.e. $J/U = 0.065$ and $W/U \approx 1$, a linearly-dispersing mode appears once more (III). We also take data deep in the disordered superfluid ($J/U = 0.1$, $W/U = 1$), showing that the superfluid is robust to the disorder strengths considered here (IV). Note that the slope of the disordered superfluid, corresponding to the speed of sound c_s of the phonon mode, is depressed relative to that of the clean superfluid. This is because c_s is related to the superfluid density n_s and

the compressibility κ through $c_s^2 \sim n_s/\kappa$. Disorder is expected to reduce the superfluid density while maintaining or increasing the compressibility, thereby resulting in a suppressed speed of sound.

We conclude by constructing a phase diagram (Fig. 5C). The phase ‘boundaries’ are inferred by binarizing the data presented in earlier figures, and as such do not reflect genuine continuous phase transitions; in a finite size system, only crossovers may exist. Furthermore, the transition from the gapped Mott insulator (MI) to the gapless Bose glass (BG) is of the Griffiths type—dominated by rare-region effects—and therefore lies beyond our resolution [41]. Nonetheless, we identify three distinct regimes, each associated with a corresponding phase in the thermodynamic limit. Collectively, our results provide a clear picture of disorder-induced superfluidity. Starting from a MI, one can seed resonances with on-site disorder. The formation of particle-hole excitations is most favorable as W approaches U , as evinced both directly and indirectly through the compressibility and condensate fraction experiments. These mobile particle-hole excitations destroy the MI and temporarily keep Anderson localization at bay. For weak disorder, the resonances are confined to small ‘puddles’ or ‘grains’ of locally mobile bosons. Near the critical disorder strength, $W_c \sim U$, the puddles grow large enough to establish global phase coherence, reminiscent of granular superconductor physics.

[†] Google Quantum AI and Collaborators

N. S. Ticea^{1,2,†}, E. Portolés^{1,†}, E. Rosenberg^{1,†}, A. Schuckert^{3,†}, A. Szasz¹, P. Praneel^{1,6}, B. Kobrin¹, N. Pomata³, C. Miao^{1,5}, S. Kumar^{1,7}, E. Crane⁴, I. Drozdov^{1,8}, Y. Lensky¹, T. G. Kiely¹², S. González-García^{1,10}, D. Abanin¹, A. Abbas¹, R. Acharya¹, L. Aghababaie Beni¹, G. Aigeldinger¹, R. Alcaraz¹, S. Alcaraz¹, M. Ansmann¹, F. Arute¹, K. Arya¹, W. Askew¹, N. Astrakhantsev¹, J. Atalaya¹, R. Babbush¹, B. Ballard¹, J. C. Bardin^{1,9}, H. Bates¹, A. Bengtsson¹, M. Bigdely Karimi¹, A. Bilmes¹, S. Biloadeau¹, F. Borjans¹, A. Bourassa¹, J. Bovaird¹, D. Bowers¹, L. Brill¹, P. Brooks¹, M. Broughton¹, D. A. Browne¹, B. Buchea¹, B. B. Buckley¹, T. Burger¹, B. Burkett¹, N. Bushnell¹, J. Busnaina¹, A. Cabrera¹, J. Campero¹, H.-S. Chang¹, S. Chen¹, Z. Chen¹, B. Chiaro¹, L.-Y. Chih¹, A. Y. Cleland¹, B. Cochran¹, M. Cockrell¹, J. Cogan¹, R. Collins¹, P. Conner¹, H. Cook¹, R. G. Cortinas¹, W. Courtney¹, A. L. Crook¹, B. Curtin¹, M. Damyanov¹, S. Das¹, D. M. Debroy¹, S. Demura¹, P. Donohoe¹, A. Dunsworth¹, V. Ehimhen¹, A. Eickbusch¹, A. Moshe Elbag¹, L. Ella¹, M. Elzouka¹, D. Enriquez¹, C. Erickson¹, L. Faoro¹, V. S. Ferreira¹, M. Flores¹, L. Flores Burgos¹, S. Fontes¹, E. Forati¹, J. Ford¹, B. Foxen¹, M. Fukami¹, A. Wing Lun Fung¹, L. Fusté¹, S. Ganjam¹, G. Garcia¹, C. Garrick¹, R. Gasca¹, H. Gehring¹, R. Geiger¹, E. Genois¹, W. Giang¹, D. Gilboa¹, J. E. Goeders¹, E. C. Gonzales¹, R. Gosula¹, S. J. de Graaf¹, A. Grajales Dau¹, D. Graumann¹, J. Grebel¹, A. Greene¹, J. A. Gross¹, J. Guerrero¹, L. Le Guevel¹, T. Ha¹, S. Habegger¹, T. Hadick¹, A. Hadjikhani¹, M. C. Hamilton^{1,11}, M. Hansen¹, M. P. Harrigan¹, S. D. Harrington¹, J. Hartshorn¹, S. Heslin¹, P. Heu¹, O. Higgott¹, R. Hiltermann¹, J. Hilton¹, H.-Y. Huang¹, M. Hucka¹, C. Hudspeth¹, A. Huff¹, W. J. Huggins¹, E. Jeffrey¹, S. Jevons¹, Z. Jiang¹, X. Jin¹, C. Jones¹, C. Joshi¹, P. Juhas¹, A. Kabel¹, D. Kafri¹, H. Kang¹, K. Kang¹, A. H. Karamlou¹, R. Kaufman¹, K. Kechedzhi¹, J. Kelly¹, T. Khattar¹, M. Khezri¹, S. Kim¹, P. V. Klimov¹, C. M. Knaut¹, A. N. Korotkov¹, F. Kostritsa¹, J. M. Kreikebaum¹, R. Kudo¹, B. Kueffler¹, A. Kumar¹, V. D. Kurilovich¹, V. Kutsko¹, D. Landhuis¹, T. Lange-Dei¹, B. W. Langley¹, P. Laptev¹, K.-M. Lau¹, E. Leavell¹, J. Ledford¹, J. Lee¹, K. Lee¹, B. J. Lester¹, W. Leung¹, L. Li¹, W. Yan Li¹, M. Li¹, A. T. Lill¹, W. P. Livingston¹, M. T. Lloyd¹, L. De Lorenzo¹, E. Lucero¹, D. Lundahl¹, A. Lunt¹, S. Madhuk¹, A. Maiti¹, A. Maloney¹, S. Mandrà¹, L. S. Martin¹, O. Martin¹, E. Mascot¹, P. Masih Das¹, D. Maslov¹, M. Mathews¹, C. Maxfield¹, J. R. McClean¹, M. McEwen¹, S. Meeks¹, A. Megrant¹, K. C. Miao¹, Z. K. Minev¹, R. Molavi¹, S. Molina¹, S. Montazeri¹, C. Neill¹, M. Newman¹, A. Nguyen¹, M. Nguyen¹, C.-H. Ni¹, M. Y. Niu¹, L. Oas¹, W. D. Oliver¹, R. Orosco¹, K. Ottosson¹, A. Pagano¹, A. Di Paolo¹, S. Peek¹, D. Peterson¹, A. Pizzuto¹, R. Potter¹, O. Pritchard¹, M. Qian¹, C. Quintana¹, G. Ramachandran¹, A. Ranadive¹, M. J. Reagor¹, R. Resnick¹, D. M. Rhodes¹, D. Riley¹, G. Roberts¹, R. Rodriguez¹, E. Ropes¹, L. B. De Rose¹, E. Rosenfeld¹, D. Rosenstock¹, E. Rossi¹, D. A. Rower¹, R. Salazar¹, K. Sankaragomathi¹, M. Can Saruhan¹, K. J. Satzinger¹, M. Schaefer^{1,10}, S. Schroeder¹, H. F. Schurkus¹, A. Shahingohar¹, M. J. Shearn¹, A. Shorter¹, V. Shvarts¹, V. Sivak¹, S. Small¹, W. Clarke Smith¹, D. A. Sobel¹, B. Spells¹, S. Springer¹, G. Sterling¹, J. Suchard¹, A. Sztein¹, M. Taylor¹, J. P. Thiruraman¹, D. Thor¹, D. Timucin¹, E. Tomita¹, A. Torres¹, M. Mert Torunbalci¹, H. Tran¹, A. Vaishnav¹, J. Vargas¹, S. Vdovichev¹, B. Villalonga¹, C. Vollgraff Heidweiller¹, M. Voorhees¹, S. Waltman¹, J. Waltz¹, S. X. Wang¹, B. Ware¹, J. D. Watson¹, Y. Wei¹, T. Weidel¹, T. White¹, K. Wong¹, B. W. K. Woo¹, C. J. Wood¹, M. Woodson¹, C. Xing¹, Z. Jamie Yao¹, P. Yeh¹, B. Ying¹, J. Yoo¹, N. Yosri¹, E. Young¹, G. Young¹, A. Zalcman¹, R. Zhang¹, Y. Zhang¹, N. Zhu¹, N. Zobrist¹, Z. Zou¹, S. Boixo¹, H. Neven¹, V. Smelyanskiy¹, G. Vidal¹, E. Mueller⁶, T. I. Andersen¹, L. B. Ioffe¹, A. Petukhov^{1,8}, M. Hafezi^{3,8}, P. Roushan^{1,8}

The physics described here is relevant to a broad class of systems governed by the dirty superfluid–insulator transition, including thin films, porous media, Josephson junction arrays, and granular superconductors. This transition may also play a key role in understanding more exotic phases such as anomalous metals and the elusive Bose metal [42, 43]. We conclude by noting a suggestive parallel with the high- T_c cuprates: the superconducting (superfluid) dome in the cuprate (disordered Bose–Hubbard) phase diagram emerges from doping holes (introducing disorder) into a MI. The superconducting phase near the critical doping point has been proposed to be granular, and doping away from it is analogous to adding disorder [44].

Acknowledgments

We would like to thank M.P.A. Fisher, N. Prokof’ev, E. Berg, S. Raghu, C. Xu, V. Khemani, A. Stern, A. Vishwanath, P. Nosov, A. Pandey, A. Sarma, and N. Myerson-Jain for insightful conversations. TGK acknowledges support from the National Science Foundation under grant PHY-2309135 to the Kavli Institute for Theoretical Physics (KITP), and from the Gordon and Betty Moore Foundation through Grant GBMF8690 to the University of California, Santa Barbara.

1 Google Research, Mountain View, CA, USA

2 Department of Applied Physics, Stanford University, Stanford, California 94305, USA

3 Department of Physics, University of Maryland, College Park, MD

4 Department of Physics, King's College London, Strand, London, WC2R 2LS, UK

5 Department of Physics, Stanford University, Stanford California 94305, USA

6 School of Applied and Engineering Physics, Cornell University, Ithaca, New York 14853, USA

8 Department of Physics, University of Connecticut, Storrs, CT

9 Department of Electrical and Computer Engineering, University of Massachusetts, Amherst, MA

10 Department of Physics, University of California, Santa Barbara, CA

11 Department of Electrical and Computer Engineering, Auburn University, Auburn, AL

12 Kavli Institute for Theoretical Physics, University of California, Santa Barbara, CA

‡ These authors contributed equally to this work.

§ Corresponding authors: hafezi@umd.edu and pedramr@google.com

[1] A. J. Leggett, Superfluidity, *Reviews of Modern Physics* **71**, S318 (1999).

[2] M. P. A. Fisher *et al.*, Boson localization and the superfluid-insulator transition, *Phys. Rev. B* **40**, 546 (1989).

[3] L. Pollet *et al.*, Absence of a direct superfluid to mott insulator transition in disordered bose systems, *Phys. Rev. Lett.* **103**, 140402 (2009).

[4] N. Elstner and H. Monien, Dynamics and thermodynamics of the bose-hubbard model, *Phys. Rev. B* **59**, 12184 (1999).

[5] B. Capogrosso-Sansone *et al.*, Monte carlo study of the two-dimensional bose-hubbard model, *Phys. Rev. A* **77**, 015602 (2008).

[6] V. Gurarie *et al.*, Phase diagram of the disordered bose-hubbard model, *Phys. Rev. B* **80**, 214519 (2009).

[7] P. A. Crowell, F. W. Van Keuls, and J. D. Reppy, Onset of superfluidity in 4 He films adsorbed on disordered substrates, *Phys. Rev. B* **55**, 12620 (1997).

[8] A. Amo *et al.*, Superfluidity of polaritons in semiconductor microcavities, *Nature Physics* **5**, 805 (2009).

[9] B. Saxberg *et al.*, Disorder-assisted assembly of strongly correlated fluids of light, *Nature* **612**, 435 (2022).

[10] M. Greiner *et al.*, Quantum phase transition from a superfluid to a mott insulator in a gas of ultracold atoms, *Nature* **415**, 39 (2002).

[11] M. Zwierlein *et al.*, Direct observation of the superfluid phase transition in ultracold fermi gases, *nature* **442**, 54 (2006).

[12] B. Deissler *et al.*, Delocalization of a disordered bosonic system by repulsive interactions, *Nature physics* **6**, 354 (2010).

[13] C. D'Errico *et al.*, Observation of a disordered bosonic insulator from weak to strong interactions, *Physical review letters* **113**, 095301 (2014).

[14] J.-C. Yu, S. Bhave, L. Reeve, B. Song, and U. Schneider, Observing the two-dimensional bose glass in an optical quasicrystal, *Nature* **633**, 338 (2024).

[15] L. Koehn *et al.*, Quantum-gas microscopy of the bose-glass phase (2025), arXiv:2504.13040 [cond-mat.quant-gas].

[16] P. Russ *et al.*, Compressibility measurement of the thermal mi-bg transition in an optical lattice (2025), arXiv:2506.16466 [cond-mat.quant-gas].

[17] L. Fallani *et al.*, Ultracold atoms in a disordered crystal of light: Towards a bose glass, *Phys. Rev. Lett.* **98**, 130404 (2007).

[18] S. Söyler *et al.*, Phase diagram of the commensurate two-dimensional disordered bose-hubbard model, *Phys. Rev. Lett.* **107**, 185301 (2011).

[19] R. Yu *et al.*, Bose glass and mott glass of quasiparticles in a doped quantum magnet, *Nature* **489**, 379 (2012).

[20] C. Meldgin *et al.*, Probing the bose glass-superfluid transition using quantum quenches of disorder, *Nature Physics* **12**, 646 (2016).

[21] Y. Chen *et al.*, Qubit architecture with high coherence and fast tunable coupling, *Phys. Rev. Lett.* **113**, 220502 (2014).

[22] T. Stöferle *et al.*, *Phys. Rev. Lett.* **92**, 130403 (2004).

[23] G. K. Campbell *et al.*, Imaging the mott insulator shells by using atomic clock shifts, *Science* **313**, 649 (2006).

[24] N. Gemelke, X. Zhang, C.-L. Hung, and C. Chin, In situ observation of incompressible mott-insulating domains in ultracold atomic gases, *Nature* **460**, 995 (2009).

[25] W. Bakr *et al.*, Probing the superfluid-to-mott insulator transition at the single-atom level, *Science* **329**, 547 (2010).

[26] J. Sherson *et al.*, Single-atom-resolved fluorescence imaging of an atomic mott insulator, *Nature* **467**, 68 (2010).

[27] C. Weitenberg *et al.*, Single-spin addressing in an atomic mott insulator, *Nature* **471**, 319 (2011).

[28] M. Endres *et al.*, Observation of correlated particle-hole pairs and string order in low-dimensional mott insulators, *Science* **334**, 200 (2011).

[29] D. Wei *et al.*, Observation of brane parity order in programmable optical lattices, *Phys. Rev. X* **13**, 021042 (2023).

[30] L. Sanchez-Palencia and M. Lewenstein, Disordered quantum gases under control, *Nature Physics* **6**, 87 (2010).

[31] C. D'Errico *et al.*, Observation of a disordered bosonic insulator from weak to strong interactions, *Phys. Rev. Lett.* **113**, 095301 (2014).

[32] S. Krinner *et al.*, Superfluidity with disorder in a thin film of quantum gas, *Phys. Rev. Lett.* **110**, 100601 (2013).

[33] B. Allard *et al.*, Effect of disorder close to the superfluid transition in a two-dimensional bose gas, *Phys. Rev. A* **85**, 033602 (2012).

[34] M. White *et al.*, Strongly interacting bosons in a disordered optical lattice, *Phys. Rev. Lett.* **102**, 055301 (2009).

[35] M. Pasienski *et al.*, A disordered insulator in an optical

lattice, *Nature Physics* **6**, 677 (2010).

[36] B. Deissler *et al.*, Delocalization of a disordered bosonic system by repulsive interactions, *Nature Physics* **6**, 354 (2010).

[37] K. Fischer and J. Hertz, *Spin Glasses* (Cambridge University Press, 1993).

[38] M. Mezard, G. Parisi, and M. Virasoro, *Spin-Glass Theory and Beyond* (World Scientific, 1987).

[39] C. N. Yang, Concept of off-diagonal long-range order and the quantum phases of liquid helium and of superconductors, *Rev. Mod. Phys.* **34**, 694 (1962).

[40] A. Griffin, *Excitations in a Bose-condensed Liquid*, Cambridge Studies in Low Temperature Physics (Cambridge University Press, Cambridge, 1993).

[41] P. Sengupta and S. Haas, Quantum glass phases in the disordered bose-hubbard model, *Phys. Rev. Lett.* **99**, 050403 (2007).

[42] A. Kapitulnik *et al.*, Colloquium: Anomalous metals: Failed superconductors, *Rev. Mod. Phys.* **91**, 011002 (2019).

[43] C. o. Yang, Intermediate bosonic metallic state in the superconductor-insulator transition, *Science* **366**, 1505–1509 (2019).

[44] B. J. Ramshaw and S. A. Kivelson, Superconductivity in overdoped cuprates can be understood from a bcs perspective! (2025), arXiv:2510.25767 [cond-mat.supr-con].

[45] M. Kjaergaard, M. E. Schwartz, J. Braumüller, P. Krantz, J. I.-J. Wang, S. Gustavsson, and W. D. Oliver, Superconducting qubits: Current state of play, *Annual Review of Condensed Matter Physics* **11**, 369–395 (2020).

[46] Y. Yanay, J. Braumüller, S. Gustavsson, W. D. Oliver, and C. Tahan, Two-dimensional hard-core bose–hubbard model with superconducting qubits, *npj Quantum Information* **6**, 10.1038/s41534-020-0269-1 (2020).

[47] J. Koch, T. M. Yu, J. Gambetta, A. A. Houck, D. I. Schuster, J. Majer, A. Blais, M. H. Devoret, S. M. Girvin, and R. J. Schoelkopf, Charge-insensitive qubit design derived from the cooper pair box, *Phys. Rev. A* **76**, 042319 (2007).

[48] F. Yan, P. Krantz, Y. Sung, M. Kjaergaard, D. L. Campbell, T. P. Orlando, S. Gustavsson, and W. D. Oliver, Tunable coupling scheme for implementing high-fidelity two-qubit gates, *Phys. Rev. Applied* **10**, 054062 (2018).

[49] A. Bengtsson, A. Opremcak, M. Khezri, D. Sank, A. Bourassa, K. J. Satzinger, S. Hong, C. Erickson, B. J. Lester, K. C. Miao, A. N. Korotkov, J. Kelly, Z. Chen, and P. V. Klimov, Model-based optimization of superconducting qubit readout, *Physical Review Letters* **132**, 10.1103/physrevlett.132.100603 (2024).

[50] T. Walter, P. Kurpiers, S. Gasparinetti, P. Magnard, A. Potočnik, Y. Salathé, M. Pechal, M. Mondal, M. Oppliger, C. Eichler, and A. Wallraff, Rapid high-fidelity single-shot dispersive readout of superconducting qubits, *Phys. Rev. Appl.* **7**, 054020 (2017).

[51] T. I. Andersen, Thermalization and criticality on an analogue–digital quantum simulator, *Nature* **638**, 79 (2025).

[52] S. Bravyi, D. P. DiVincenzo, and D. Loss, Schrieffer–wolff transformation for quantum many-body systems, *Annals of physics* **326**, 2793 (2011).

[53] M. Hörmann and K. P. Schmidt, Projective cluster-additive transformation for quantum lattice models, *SciPost Physics* **15**, 097 (2023).

[54] S. R. White, Density matrix formulation for quantum renormalization groups, *Phys. Rev. Lett.* **69**, 2863 (1992).

[55] S. R. White, Density-matrix algorithms for quantum renormalization groups, *Phys. Rev. B* **48**, 10345 (1993).

[56] U. Schollwöck, The density-matrix renormalization group in the age of matrix product states, *Annals of Physics* **326**, 96 (2011).

[57] Technically, it should be $\kappa = \frac{1}{n^2} (\partial n / \partial \mu)$, where n is the average filling; in our case, $n = 1$.

[58] B. Foxen *et al.* (Google AI Quantum), Demonstrating a continuous set of two-qubit gates for near-term quantum algorithms, *Phys. Rev. Lett.* **125**, 120504 (2020).

[59] R. P. Feynman, Atomic theory of the two-fluid model of liquid helium, *Phys. Rev.* **94**, 262 (1954).

[60] K. Sheshadri, H. R. Krishnamurthy, R. Pandit, and T. V. Ramakrishnan, Superfluid and insulating phases in an interacting-boson model: Mean-field theory and the rpa, *Europhysics Letters* **22**, 257 (1993).

[61] D. van Oosten, D. B. M. Dickerscheid, B. Farid, P. van der Straten, and H. T. C. Stoof, Inelastic light scattering from a mott insulator, *Phys. Rev. A* **71**, 021601 (2005).

[62] C. Trefzger, C. Menotti, and M. Lewenstein, Ultracold dipolar gas in an optical lattice: The fate of metastable states, *Phys. Rev. A* **78**, 043604 (2008).

[63] K. V. Krutitsky and P. Navez, Excitation dynamics in a lattice bose gas within the time-dependent gutzwiller mean-field approach, *Phys. Rev. A* **84**, 033602 (2011).

[64] E. Altman and A. Auerbach, Oscillating superfluidity of bosons in optical lattices, *Phys. Rev. Lett.* **89**, 250404 (2002).

[65] S. D. Huber, E. Altman, H. P. Büchler, and G. Blatter, Dynamical properties of ultracold bosons in an optical lattice, *Phys. Rev. B* **75**, 085106 (2007).

[66] S. Östlund and S. Rommer, Thermodynamic limit of density matrix renormalization, *Phys. Rev. Lett.* **75**, 3537 (1995).

[67] J. Haegeman, C. Lubich, I. Oseledets, B. Vandereycken, and F. Verstraete, Unifying time evolution and optimization with matrix product states, *Phys. Rev. B* **94**, 165116 (2016).

[68] S. Paeckel, T. Köhler, A. Swoboda, S. R. Manmana, U. Schollwöck, and C. Hubig, Time-evolution methods for matrix-product states, *Annals of Physics* **411**, 167998 (2019).

[69] C. Hubig, I. P. McCulloch, and U. Schollwöck, Generic construction of efficient matrix product operators, *Phys. Rev. B* **95**, 035129 (2017).

[70] T. E. Baker, A. Foley, and D. Sénéchal, Direct solution of multiple excitations in a matrix product state with block Lanczos, *Eur. Phys. J. B* **97**, 72 (2024), arXiv:2109.08181 [cond-mat.str-el].

Supplementary Materials for “Disorder-induced superfluidity”

Google Quantum AI and collaborators[†] and Google Quantum AI and Collaborators
(Dated: December 29, 2025)

Contents

References	7
I. Transmon-Based Realization of the Bose-Hubbard Model	2
II. Qutrit Calibration	3
III. Device modeling	3
IV. State preparation	5
V. Compressibility	6
A. Definition	6
B. Fluctuation-dissipation derivation	6
C. Relation to dynamical structure factor	7
D. Protocols for measurement	7
VI. Single Particle Density Matrix (Two-Point Correlator)	8
A. Definition	8
B. Protocol for measurement	9
C. Accounting for phase offset	9
D. Benchmarking	11
VII. Dynamical structure factor	11
A. Definition	11
B. Feynman-Bijl Ansatz	12
C. Inhomogeneous system	15
D. Calculating the dynamical structure factor with Feynman-Bijl ansatz	16
VIII. Calculating excitation spectrum using Gutzwiller ansatz	18
IX. Matrix product state simulations	20
A. Simulation types	20
B. Results for various observables	21
C. Insights from comparison between experiment and simulation	23

I. Transmon-Based Realization of the Bose-Hubbard Model

As reviewed in [45, 46], there are a large number of superconducting qubit architectures, all of which are suitable for implementing the Bose-Hubbard model. The building block of our processor is a tunable transmon depicted in Fig. S1. In its simplest incarnation it is comprised of two Josephson junctions shunted with a capacitor. The Hamiltonian of a single transmon can be approximated by that of the anharmonic Duffing oscillator [47] with eigenstates labeled by an integer n , corresponding to an energy $E_n = \hbar\omega(n + 1/2) + (\eta/2)n(n - 1) + \dots$, where the neglected terms are higher order in n . This, in turn, can be viewed as a Bose-Hubbard Hamiltonian in the atomic limit with Hubbard energy equal to the transmon anharmonicity η . Thus, a transmon is a multi-level system (qudit) with Bose operators \hat{a} and \hat{a}^\dagger connecting the states in its Hilbert space: $\hat{a}|n\rangle = \sqrt{n}|n-1\rangle$, $\hat{a}^\dagger|n\rangle = \sqrt{(n+1)}|n\rangle$. We interpret n as the number of bosons (microwave photons) on a site, and introduce the number operator satisfying $\hat{n}|n\rangle = n|n\rangle$. The capacitive coupling between the qudits generates the hopping terms. The main feature of our analog simulator is that it utilizes tunable couplers. As a result, the kinetic part of the Bose-Hubbard Hamiltonian can be controlled in the broad range by an external flux bias.

A simplified circuit diagram of a dimer formed by a pair of nearest neighbor transmons is shown in Fig. S1. The qudits 1 and 2 interact with each other via another transmon (coupler), which is capacitively coupled to both of them. There is also a small direct coupling between the neighboring transmons, which is necessary to turn off the effective coupling. Both the qudit frequencies ω_i and the coupler frequency ω_c are controllable via the external fluxes, Φ_i and Φ_c [47]. The effective coupling g developed between the two qudits is given by [48]

$$g \simeq \left(k_d - k_1 k_2 \frac{\omega_q^2}{\omega_c^2 - \omega_q^2} \right) \frac{\sqrt{\omega_1 \omega_2}}{2}, \quad (\text{S1})$$

where $\omega_q = (\omega_1 + \omega_2)/2$ and dimensionless parameters k_d and k_i are so-called coupling efficiencies that are functions of the circuit capacitances (Fig. S1). The coupler operates in the regime when $\omega_c \gg \omega_{1,2}$, i.e. it remains unpopulated

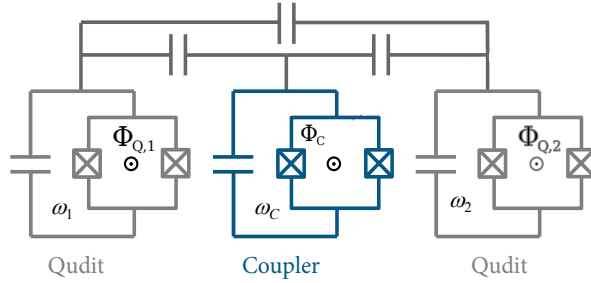


FIG. S1. Schematic circuit diagram of a transmon dimer with a tunable coupler.

and serves only to mediate the coupling between the qubits. The idle frequency of the coupler is given by

$$\omega_c^{\text{off}} = \omega_q \sqrt{1 + k_1 k_2 / k_d}, \quad (\text{S2})$$

which corresponds to $g = 0$ in Eq. (S1). Therefore when $\omega_c > \omega_c^{\text{off}}$ the effective coupling $g < 0$.

By coupling transmons, as illustrated in Fig. S1, one can realize an effective lattice in which the local bosons tunnel between lattice sites. One distinct advantage of this architecture is its flexibility: graphs of various connectivity may be constructed with turning appropriate couplers “on” and “off”. To make connection with Bose-Hubbard Hamiltonian in Eq. (1) of the main text we express transmon frequencies as $\omega_i = \omega_q + \delta_i$, where ω_q is the reference (interaction) frequency when all transmons are on resonance. While the full circuit in Fig. S1 does not conserve total boson number, the non-conserving processes are far off resonance and may be ignored in an effective rotating-wave approximation since $\omega_q \gg |g|$. After transforming into a rotating frame with frequency ω_q and neglecting off-resonant counter-rotating terms, the Hamiltonian for an array of transmons wired in a circuit reads:

$$\mathcal{H}_{\text{BH}} = g \sum_{\langle i,j \rangle} (a_i^\dagger a_j + \text{H.c.}) + \frac{\eta}{2} \sum_i n_i(n_i - 1) + \sum_i \delta_i n_i. \quad (\text{S3})$$

Here i indexes the transmons, and operators a_i, a_i^\dagger , and $\hat{n}_i = a_i^\dagger a_i$ are raising, lowering and number operators for the i ’th transmon. The first term encodes coupling between connected nearest-neighbors. The non-linearity, $\eta < 0$

is fixed. For state preparation and measurements one can also send microwave signals into the circuit which drive transitions, $H_{\text{ext}} = \sum_i (\Omega_i(t)\hat{a}_i + \Omega_i^*(t)\hat{a}_i^\dagger)$.

Comparing with Eq. (1) of the main text, we see that the coupled transmons reproduce the Bose-Hubbard model if we identify $J = -g$, $\mu_i = -\delta_i$, $U = \eta$. Note that under this mapping, the Hubbard interaction U is negative but much of the interesting Bose-Hubbard physics requires $U > 0$. The thermodynamic properties of the Bose-Hubbard model with an attractive interaction are dramatically different from that of the repulsive model. In particular, the ground state of lattice bosons with an attractive interaction will exhibit a collapse: all bosons will seek to localize on a single lattice site. In the absence of a heat-bath, however, the sign of U is largely irrelevant. Due to time-reversal symmetry one can map time evolution with a Hamiltonian H onto evolution under $-H$. The transformation $H \rightarrow -H$ flips the sign of U . It also flips the signs of g and δ_i . On a bipartite lattice the sign of g can be restored via a gauge transformation, and δ_i is under experimental control. Thus one can use experiments on Hamiltonian (S3) with $\eta < 0$ to learn about the physics of Eq. (1) in the main text with $U > 0$. This connection between experiments involving H and $-H$ is perhaps even more clear in the spectral domain. The eigenstates of H and $-H$ are the same after taking $E \rightarrow -E$. Thus the ground state of H maps onto the highest excited state of $-H$ and one can use the adiabatic theorem to produce this highest energy state starting from the product state $|11\dots11\rangle$ when $g = 0$, and then adiabatically modulating g and possibly δ_i as needed.

II. Qutrit Calibration

In order to control and readout the $|2\rangle$ state of our transmons, we have adapted the existing software infrastructure for the $(|0\rangle, |1\rangle)$ subspace. To begin with, we perform the same set of calibrations for control pulses as for the $|0\rangle \leftrightarrow |1\rangle$ transition, but for the $|1\rangle \leftrightarrow |2\rangle$ transition. We follow by calibrating the readout protocol to distinguish between the $|0\rangle$, $|1\rangle$ and $|2\rangle$ states. To this end, we adapted the optimization routine described in Ref. [49] by factoring in the readout fidelity of the 2 state in the cost function of the routine. The primary trade-off is in the length of the readout pulse. Indeed, when optimizing for readout fidelities, one wants to make the readout tone as long as possible to maximize the signal-to-noise ratio (SNR), but short enough to not be affected by T1 errors [50]. Because the T1 of the $|1\rangle$ state and the $|2\rangle$ state differs by $\sqrt{2}$, there is no common optimal point, and fidelity in detecting one state always comes at the expense of a decrease in that of the other. Finally, the analog evolution part of the experimental procedure requires a precise calibration, detailed in Ref. [51]. No difference in this calibration procedure is required for operating the $|2\rangle$ state.

III. Device modeling

In this section, we describe our approach for accurate device calibration and modeling, building upon the techniques introduced in Ref. [51]. Crucially, our analysis incorporates high-order, coupler-mediated processes that generate effective interactions beyond the standard Bose-Hubbard model discussed in Section I. These high-order corrections become increasingly significant at larger effective coupling strengths, J ; as such, they are important for providing an accurate description of the emergent superfluid phase. In Section IX, we numerically simulate the experimental sequences in this work under the full effective Hamiltonians (Eq. S5) and quantify the impact of the higher-order corrections on the relevant physical observables.

Bare parameter calibration: As in Ref. [51], we begin by modeling the *bare* Hamiltonian of our device as a set of coupled transmons:

$$H_{\text{bare}} = \sum_{i \in Q, C} \left(\omega_i a_i^\dagger a_i + \frac{\eta_i}{2} a_i^\dagger a_i^\dagger a_i a_i \right) + \sum_{i, j \in Q, C} \frac{k_{ij}}{2} \sqrt{\omega_i \omega_j} (a_i + a_i^\dagger)(a_j + a_j^\dagger) \quad (\text{S4})$$

where a_i are bosonic operators acting on the combined set of qubits and couplers, ω_i are the frequencies, η_i are the anharmonicities, and k_{ij} are the capacitive coupling efficiencies. For the coupling efficiencies, we include nearest-neighbor qubit-qubit and qubit-coupler couplings (as depicted in Fig. S1), as well as next-nearest-neighbor qubit-qubit and coupler-coupler which arise in larger-scale circuits.

The parameters in this model (k_{ij} , η_i and ω_i) are determined through a combination of spectroscopy experiments and device modeling, following the procedures established in Ref. [51]. While k_{ij} and η_i are static parameters intrinsic to the device fabrication, the frequencies ω_i are calibrated for a specified experimental sequence to set the nearest-neighbor interaction strength, $|J|$, and onsite disorder.

Effective modeling: Having characterized the bare device Hamiltonian, we turn to deriving an *effective* Hamiltonian acting only on the qubit degrees of freedom. This simplification is motivated by two key properties: (i) the large detuning between qubits and couplers (\sim GHz) relative to their coupling strength (\sim 100 MHz) ensures weak hybridization, and (ii) the activation of the coupling via gradual ramps (on the order of a few nanosecond) ensures that the qubits remain within the “dressed” basis.

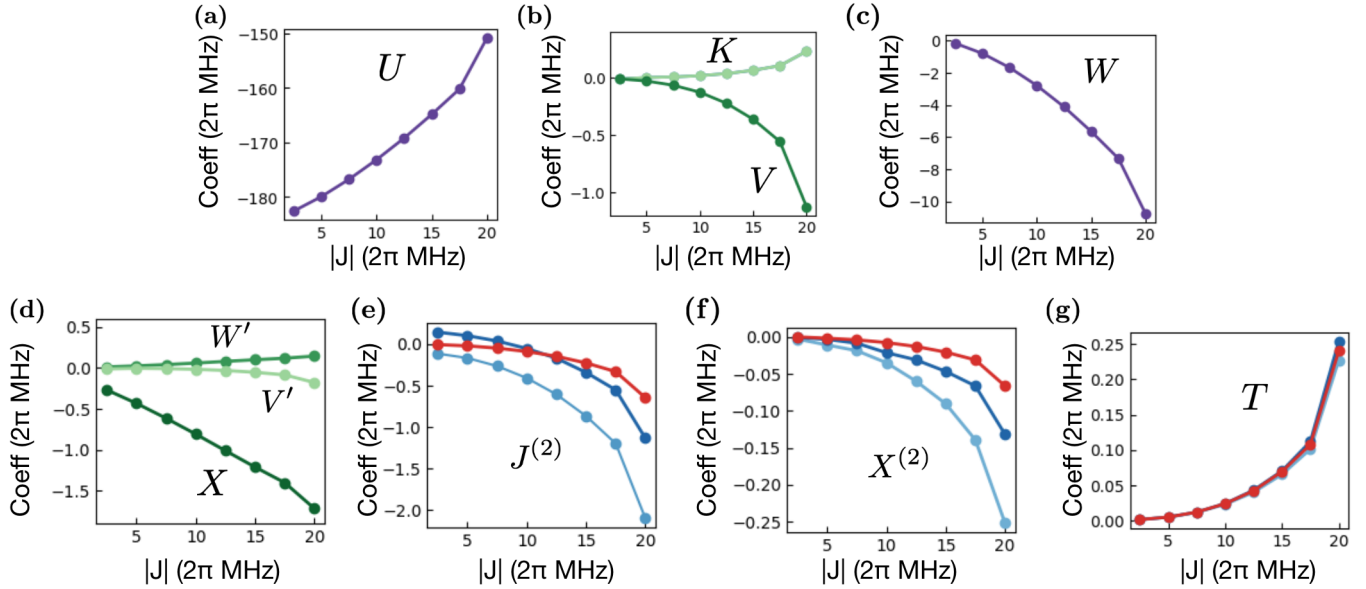


FIG. S2. Average coefficients in the extended Bose-Hubbard Hamiltonian, Eq. S5, as a function of $|J|$ for (a) 2-body onsite interactions, U ; (b) density-density nearest-neighbor interactions, V and K ; (c) 3-body onsite interactions, W ; (d) density-dependent nearest-neighbor hoppings, X, V' , and W' ; (e) next-nearest neighbor hoppings, $J^{(2)}$; (f) next-nearest neighbor density-dependent hoppings, $X^{(2)}$; and (g) density-mediated 3-site hoppings. For (f) and (g), we plot the three relative next-nearest-neighbor orientations: along the two diagonal directions (light, dark blue) and along a line (red). For (h), the hopping occurs between next-nearest sites along the same three orientations and the density operator acts on site in the middle.

To perform the effective modeling, we introduce a scalable technique which has not previously been applied to superconducting-qubit architectures: the exact *Schrieffer-Wolff (SW) transformation* combined with a *linked-cluster expansion*. The exact SW transformation—also known as the direction rotation—is defined as the minimal unitary rotation, U , that maps the “dressed” subspace P onto the unperturbed subspace P_0 [52]. One can derive U by numerically diagonalizing the full Hamiltonian H and identifying the eigenstates that exhibit maximal overlap with the unperturbed states of P_0 . However, because of the high computational cost of exact diagonalization, this implementation is generally restricted to small-scale systems. To overcome this limitation, we incorporate the Schrieffer-Wolff transformation within a linked-cluster expansion framework. First, we compute the effective Hamiltonians on a set of small, overlapping linked clusters through an exact SW transformation. Then, by summing the individual cluster Hamiltonians (via the inclusion-exclusion principle), we construct a global effective Hamiltonian for the full system [53]. This combined approach ensures a computational cost that scales linearly with the system size while maintaining a high degree of accuracy. By performing the exact SW transformation locally, we incorporate all high-order virtual processes within the support of each cluster. Meanwhile, long-range effects are systematically captured by forming clusters that reflect the device’s interaction geometry.

More concretely, we define linked clusters to be sets of transmons—qubits or clusters—in which each transmon is adjacent to at least one other transmon in the cluster. We perform the cluster expansion for clusters up to size of $k = 7$, where the cluster size k is defined as the total number of transmons within the cluster. For each cluster C_i , we derive the effective Hamiltonian $H_{\text{eff}}(C_i)$ in the following way:

- We isolate the bare cluster Hamiltonian $H_{\text{bare}}(C_i)$ with support on C_i and truncate onto states with up to 4 excitations per qubit, 3 excitations per coupler, and 7 excitations in total.
- We perform the exact SW transformation on $H_{\text{bare}}(C_i)$ with respect to qubit manifolds with conserved total particle number, n . Namely, we determine the direct rotation that corresponds to states with n total excitations in the qubits and no excitations in the couplers.
- We combine the effective Hamiltonians for up to $n = 3$ to construct a particle-conserving effective cluster Hamiltonian, $H_{\text{eff}}(C_i)$.

By summing the effective cluster Hamiltonians, we derive a global effective Hamiltonian with up to 3-body bosonic terms on 4 adjacent qubits. As expected for a well-controlled cluster expansion, we observe that the terms in the

effective model converge as a function of cluster size; by tracking this convergence, we estimate an accuracy of $\lesssim 10$ kHz per term.

The resulting effective models are described by the following extended Bose-Hubbard Hamiltonian:

$$\begin{aligned}
H_{\text{eff}} = & - \sum_{\langle i,j \rangle} J_{ij} (a_i^\dagger a_j + a_j^\dagger a_i) - \sum_i \mu_i n_i + \sum_i \frac{U_i}{2} n_i (n_i - 1) \\
& + \sum_{\langle i,j \rangle} V_{ij} n_i n_j + \sum_{\langle i,j \rangle} K_{ij} [n_i (n_i - 1) n_j + h.c.] + \sum_i \frac{W_i}{6} n_i (n_i - 1) (n_i - 2) \\
& - \sum_{\langle i,j \rangle} X_{ij} [a_i^\dagger (n_i + n_j) a_j + h.c.] - \sum_{\langle i,j \rangle} V'_{ij} [a_i^\dagger n_i n_j a_j + h.c.] - \sum_{\langle i,j \rangle} W'_{ij} (a_i^\dagger [n_i (n_i - 1) + n_j (n_j - 1)] a_j + h.c.) \\
& - \sum_{\langle\langle i,j \rangle\rangle} J_{ij}^{(2)} (a_i^\dagger a_j + a_j^\dagger a_i) - \sum_{\langle\langle i,j \rangle\rangle} X_{ij}^{(2)} [a_i^\dagger (n_i + n_j) a_j + h.c.] - \sum_{\langle i,j,k \rangle} T_{ijk} n_i (a_j^\dagger a_k + a_k^\dagger a_j)
\end{aligned} \tag{S5}$$

The first line contains terms that appear in the leading-order analysis described in Section I. These include: density-density interactions on nearest-neighbor sites (V and K); three-body onsite interactions (W); density-dependent corrections to the nearest-neighbor hoppings (X , V' and W'); direct and density-dependent hoppings between next-nearest-neighbor sites ($J^{(2)}$ and $X^{(2)}$); and density-mediated hoppings among three adjacent sites (T). While the effective Hamiltonian contains higher-order terms beyond those explicitly listed, we find their contributions to be negligible on the physical observables of interest.

In Fig. S2, we plot the average coefficient for each term in the above Hamiltonian for a 36-qubit subsystem as a function of the nearest-neighbor hopping strength, $|J|$. Most notably, we observe strong corrections in the Hubbard interaction (U) compared to the intrinsic qubit anharmonicity ($\eta/(2\pi) \approx 190$ MHz). These corrections arise from a dispersive shift between an adjacent qubit and coupler that occurs at the same order as the interaction J itself (i.e. g_{qc}^2/Δ where $g_{qc} = k_{qc}/2\sqrt{\omega_q \omega_c}$ and $\Delta = |\omega_c - \omega_q|$). Other terms that vary linearly in J are the density-dependent two-site hopping X and the three-body onsite term W . The remaining terms originate from higher-order perturbative processes; consequently, their magnitudes increase non-linearly in $|J|$ and diminish rapidly as a function of both interaction order (e.g. 3-body vs. 2-body) and spatial distance (e.g. next-nearest-neighbor vs. nearest-neighbor).

IV. State preparation

In this section we will describe our protocol for preparing low-energy states, as well as our estimates of the energy density and (where applicable) effective temperature of the system. At time $t = 0$ all of the couplers are turned off, and a simple product state $|\psi(t=0)\rangle = |1\rangle \otimes |1\rangle \otimes \dots \otimes |1\rangle$ is prepared. This state is close to the ground state of the system when J is small (Mott insulator). Next, we slowly turn on the couplers to prepare an interacting state. In order for the low-energy product state to remain adiabatically connected to the interacting ground state, the length of the ramp (t_{ramp}) must satisfy

$$\frac{1}{t_{\text{ramp}}} \ll \Delta_E, \tag{S6}$$

where Δ_E is the many-body gap. A ramp time of 50ns is sufficient to satisfy this condition. We estimate the energy of our final state by measuring the expectation value of the Hamiltonian:

$$E \equiv \langle H \rangle = -J \sum_{\langle ij \rangle} \langle a_i^\dagger a_j + a_j^\dagger a_i \rangle + \frac{U}{2} \sum_i \langle n_i (n_i - 1) \rangle + \sum_i \mu_i \langle n_i \rangle \tag{S7}$$

We then compare our energy measurement to that predicted using tensor network numerics. The discrepancy in energy is plotted in Fig. S3. We find that the difference in energy between the target state and the prepared state is far below that of the Mott gap $\sim U$.

Much of the discrepancy can be explained by the fact that an instantaneous quench is not possible on the real device, and the correlations and doublon population change substantially while the couplings are ramped off before measurement. We show in the figure that the contribution of nearest-neighbor correlators to the energy density at each J/U is much closer to the experimentally measured value when we include a 1 ns ramp-down after adiabatic state preparation; the true ramp-down time is likely slightly longer, which would further reduce the correlations. Note that just changing from ground state search to adiabatic state preparation (with no ramp-down) in the simulation has very little effect, so the ramp-down is the key difference. See Sec. IX for more details on the simulations. Thus the adiabatically prepared state is closer to the ground state than it appears from the final measured energy density.

State preparation in the presence of disorder is hampered by the existence of metastable states. Although it is not

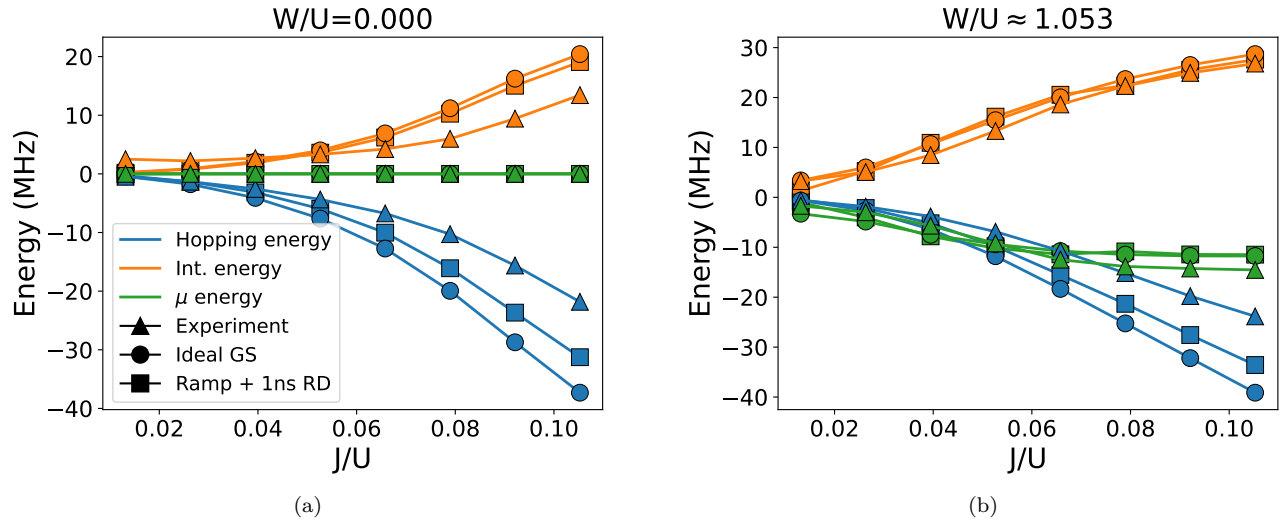


FIG. S3. We compare the energy density measured in the experiment with that predicted by tensor network numerical simulations (described in Sec. IX below), both (a) in the disorder-free case, $W = 0$, and (b) for $W/(2\pi) = 200$ MHz. The orange lines correspond to interaction energy (U term in the Hamiltonian), the blue lines to energy from nearest neighbor correlators, $\langle a_i^\dagger a_j \rangle$, and the green lines to energy from fluctuations in particle number $\langle n \rangle$ across the chip. The latter is exactly 0 in the disorder-free case but is significant when disorder is nonzero. The experimental energy density is compared with energy computed in the ideal target ground state (circles), as found using well-converged density matrix renormalization group (DMRG) simulations [54–56]. We also show the results of simulating adiabatic state preparation followed by a fast 1 ns ramp-down of the coupling (squares), close to the procedure used in the actual experiment. This gives a closer agreement with the experimental energy density, while simulating just adiabatic state preparation (not shown) gives good agreement with the true ground state. Taken together, these data suggest that we indeed prepare a very good approximation to the target state through our adiabatic state preparation procedure.

entirely possible to prevent the system from settling into a metastable configuration during the adiabatic ramping, we find that the optimal state preparation protocol is one in which (1) we first bring the qutrits to a common interaction frequency with no disorder, and then (2) turn on the inter-site coupling and disorder potential at the same time and rate. This second step is performed adiabatically.

V. Compressibility

A. Definition

The compressibility, defined [57]

$$\kappa = \frac{\partial n}{\partial \mu}, \quad (S8)$$

is an indication of how the system responds to a change in the chemical potential, μ . An incompressible system is one in which there is no local change in the particle density in response to a local change in the potential. This is characteristic of an insulator. Conversely, a compressible system will rearrange its particle density to respond to spatial gradients in the potential. The compressibility can be equivalently thought of as an indication of whether or not there is a gap to the ground state; a gapless system does not incur an energetic penalty for adding another particle (and therefore $1/\kappa$ is small), whereas for a gapped system the energetic cost for adding a new particle is large and approximately equal to the interaction strength U .

B. Fluctuation-dissipation derivation

Allow us to derive a relationship between the compressibility and the particle-number variance using the fluctuation-dissipation theorem (FDT). We will then argue that this relationship is not valid in the presence of disorder, and propose an alternative scheme for measuring κ . We begin with the observation that, for a system with Hamiltonian H in thermal equilibrium with an additive constant of the motion X , the grand canonical ensemble can be written down as

$$\Omega = -T \log \mathcal{Z}; \quad \mathcal{Z} = \text{Tr} \left[e^{-\beta H'} \right]; \quad H' = H - \lambda X, \quad (S9)$$

where λ is some Lagrange multiplier that controls the distribution over X under the ensemble. The FDT tells us that fluctuations of X in a volume with linear size much larger than all correlation scales is described by a Gaussian distribution,

$$P(X) \propto e^{\frac{(X - \bar{X})^2}{2C^2}}, \quad (\text{S10})$$

where \bar{X} is the mean of the distribution and C is the variance. These parameters can be extracted directly from the grand canonical ensemble using the following relations:

$$\bar{X} = -\frac{\partial \Omega}{\partial \lambda}; \quad C^2 = \langle (X - \bar{X})^2 \rangle = -T \frac{\partial^2 \Omega}{\partial^2 \lambda} \quad (\text{S11})$$

We now apply it to the case of particle number conservation, where $X = \hat{N}$ and $\lambda = \mu$. From this, we find

$$\begin{aligned} \langle N^2 \rangle - \langle N \rangle^2 &= -T \frac{\partial}{\partial \mu} \left(-\frac{\partial \Omega}{\partial \mu} \right) \\ &= T \frac{\partial \langle N \rangle}{\partial \mu} \\ &= TV \frac{\partial \langle n \rangle}{\partial \mu} \end{aligned} \quad (\text{S12})$$

It follows, then, that the compressibility is related to particle-number fluctuations in the following manner:

$$\kappa_T = \frac{1}{VT} (\langle N^2 \rangle - \langle N \rangle^2) \quad (\text{S13})$$

This relation applies to a system in thermal equilibrium. We plot the particle-number variance as a function of J and W in Fig. 2B of the main text. However, in a non-thermalizing system—such as a glass—one cannot apply the FDT because there is no notion of temperature. As a result, one must devise an alternative scheme for measuring the compressibility.

C. Relation to dynamical structure factor

We will use as our starting point the linear response relationship between density n and external potential ϕ , with χ^R the dynamical structure factor:

$$\delta n = \chi^R(\mathbf{q}, \omega) \phi_{\text{ext}}(\mathbf{q}, \omega), \quad (\text{S14})$$

where χ^R is the dynamical structure factor. Consider the following static modulation of the potential:

$$\phi_{\text{ext}}(\mathbf{q}, \omega) = \delta\mu \delta^2(\mathbf{q}) \delta^2(\omega) \quad (\text{S15})$$

In real space, this would correspond to a flat shift, $\delta\mu$, of the chemical potential across all space. The linear response relationship would then give us

$$\lim_{\mathbf{q} \rightarrow 0} \chi^R(\mathbf{q}, 0) = \frac{\delta n}{\delta \mu} \equiv \kappa, \quad (\text{S16})$$

which is just the compressibility. In a finite-size system, the $\mathbf{q} \rightarrow 0$ limit is inaccessible, and so we focus on calculating $\chi^R(\mathbf{q}_{\min}, 0)$, where $q_{x,\min} = \pi/L_x$ is the smallest wavevector that can be supported on the device (for the data presented in the paper, $L_x = 9$). The compressibility is therefore approximated as

$$\kappa \approx \frac{2}{N\delta\mu} \sum_j \langle n_j \rangle \cos\left(\frac{x_j\pi}{L}\right) \quad (\text{S17})$$

D. Protocols for measurement

The average in Eq. S17 has not been rigorously defined yet. Let us consider first the case where there is no disorder in the system. Assuming that the system has thermalized, $\langle n_j \rangle$ is well-defined; it is the average of the local density operator n_j with respect to the equilibrium ensemble. At $T = 0$, this is just the ground state. Formally, for some arbitrary operator \hat{X} ,

$$\langle X \rangle = \text{Tr}[\rho_{\text{eq}} \hat{X}] \quad (\text{S18})$$

Now, let us consider what happens if disorder is present. If the system is glassy, as would be expected in the regime of intermediate to strong disorder, then the system will fail to equilibrate as a result of slow dynamics. In this case, the

average $\langle X \rangle$ is not over the equilibrium ensemble, but rather some more complicated ensemble reflecting the states near whatever metastable configuration the system is presently in. Formally,

$$\langle X \rangle_{\text{glass}} = \text{Tr}[\rho_{\text{meta}} \hat{X}], \quad (\text{S19})$$

where we use the notation ρ_{meta} to reflect the ensemble of states around the local metastable minimum in which the system resides. Naturally, ρ_{meta} is path-dependent; there is some notion of the system's 'history' in phase space. With this knowledge, we can therefore suggest two distinct protocols for preparing ρ_{meta} , each of which map onto experimental paradigms in classical glasses. We summarize them below:

- **Zero-field cooled (ZFC):** Prepare the state with disorder and then apply the cosine tilt to the potential
- **Field cooled (FC):** Apply the cosine tilt first and then turn on the couplers

In the absence of disorder, these protocols should yield the same value for the compressibility. This is because $\rho_{\text{ZFC}} = \rho_{\text{FC}} = \rho_{\text{eq}}$. But if the system enters a non-ergodic regime, then by definition it will no longer explore the full phase space, and $\rho_{\text{ZFC}} \neq \rho_{\text{FC}} \neq \rho_{\text{eq}}$. Therefore, $\langle X \rangle_{\text{ZFC}} \neq \langle X \rangle_{\text{FC}}$. This is a useful diagnostic for non-ergodicity.

Finally, allow us to address some practical considerations. First, one might be concerned that initializing a state with a tilted potential will create resonances in the system, thus destroying the Mott insulator even for very small values of coupling J . However, the time-scale associated with this process should be $\tau \sim \frac{1}{J^L}$, which is very slow assuming small J . Furthermore, we can always make the tilt small enough to prevent any resonances from appearing. We take $\delta\mu = 30$ MHz, which we confirm to be in the regime of linear response.

Furthermore, to ensure that the random disorder configuration itself is not contributing any spurious potential tilt, we subtract away any residual tilt in the following manner:

$$\begin{aligned} V_i &= \mu_i + h_i + (\delta\mu - A) \cos(\pi x_i/L); \\ A &\equiv \frac{2}{N} \sum_i h_i \cos(\pi x_i/L) \end{aligned} \quad (\text{S20})$$

where V_i is the total potential felt at site \mathbf{r}_i and h_i is the local modification to the chemical potential due to disorder.

VI. Single Particle Density Matrix (Two-Point Correlator)

A. Definition

A Bose-Einstein condensate (BEC) is characterized by the macroscopic occupation of the zero-momentum eigenstate:

$$\langle a^\dagger(\mathbf{k} = 0) a(\mathbf{k} = 0) \rangle_0 = N_0 \quad (\text{S21})$$

such that $n_0 = N_0/V$, the fraction of particles participating in the condensate, remains finite in the thermodynamic limit. (The notation $\langle \dots \rangle_0$ means that we take the expectation value with respect to the non-interacting system.) Formally, a condensate is a state in which the single-particle density matrix (SPDM) does not vanish at large separation $|\mathbf{r} - \mathbf{r}'|$:

$$C_{\mathbf{r}, \mathbf{r}'} \equiv \frac{1}{\Omega} \langle a^\dagger(\mathbf{r}) a(\mathbf{r}') \rangle; \quad \lim_{|\mathbf{r} - \mathbf{r}'| \rightarrow \infty} C_{\mathbf{r}, \mathbf{r}'} \neq 0 \quad (\text{S22})$$

One normally expects the correlators to factorize in the limit $|\mathbf{r} - \mathbf{r}'| \rightarrow \infty$ since fluctuations at locations \mathbf{r} and \mathbf{r}' become independent of each other. This means that

$$\lim_{|\mathbf{r} - \mathbf{r}'| \rightarrow \infty} \langle a^\dagger(\mathbf{r}) a(\mathbf{r}') \rangle = \lim_{|\mathbf{r} - \mathbf{r}'| \rightarrow \infty} \langle a^\dagger(\mathbf{r}) \rangle \langle a(\mathbf{r}') \rangle \neq 0 \quad (\text{S23})$$

This result implies that the expectation of the field operators acquires a finite value:

$$\begin{aligned} \langle a^\dagger(\mathbf{r}) \rangle &\neq 0 \\ \langle a(\mathbf{r}) \rangle &\neq 0 \end{aligned} \quad (\text{S24})$$

Assuming translational invariance, we may take the Fourier transform of the single-particle density matrix:

$$\lim_{\mathbf{k} \rightarrow 0} C_{\mathbf{k}} = \lim_{\mathbf{k} \rightarrow 0} \frac{1}{\Omega} \langle a^\dagger(\mathbf{k}) \rangle \langle a(\mathbf{k}) \rangle = n_0, \quad (\text{S25})$$

To arrive at the last equality we used Eq. S21 assuming the formation of a condensate. One can now make the following identification:

$$\lim_{\mathbf{k} \rightarrow 0} |\langle a^\dagger(\mathbf{k}) \rangle| = \lim_{\mathbf{k} \rightarrow 0} |\langle a(\mathbf{k}) \rangle| = \sqrt{n_0} \quad (\text{S26})$$

The quantity n_0 is the condensate fraction. The existence of a finite condensate fraction is a defining property of a Bose-Einstein condensate because it implies the presence of off-diagonal long-range order, and therefore phase coherence. As we describe below, we have developed a procedure for measuring the SPDM in real space, $C_{\mathbf{r},\mathbf{r}'}$. To find n_0 , we simply diagonalize $C_{\mathbf{r},\mathbf{r}'}$ and take the leading eigenvalue, which corresponds to the occupation of the most-populated mode (i.e., that corresponding to the smallest k value, which for a system of linear dimension L is $k_{\min} = \pi/L$). If n_0 is of order N , the total number of particles in the system, then one can claim the existence of a condensate. We note that this procedure works also for disordered systems after translational invariance is restored by disorder averaging. However, the condensate wavefunction (the eigenstate corresponding to the largest eigenvalue) may exhibit spatial fluctuations that are correlated with the disorder.

B. Protocol for measurement

Because our bosonic creation and annihilation operators a^\dagger, a live in qutrit space, we cannot straightforwardly measure the two-point correlator $C_{ij} \equiv \langle a_i^\dagger a_j \rangle$ using our processor, which can only record shots of the population $n_i = a_i^\dagger a_i$. To this end, we develop a tomography protocol that relies on first rotating the state vector $\Psi \rightarrow \Psi_{R(\varphi)}$, then measuring the population. The relationship between the population measurement in the rotated state and the two-point correlator is

$$\langle \Psi_{R(\varphi)} | (n_i - 1)(n_j - 1) | \Psi_{R(\varphi)} \rangle = \frac{2}{3} C_{ij} \cos(\varphi - \phi_{ij}), \quad (\text{S27})$$

where ϕ_{ij} is the difference in phase, $\phi_i - \phi_j$, between sites i and j . Therefore, to measure C_{ij} , we simply sweep φ and then fit our data. Let us now derive an expression for the rotated state vector $\Psi_{R(\varphi)}$ and motivate Eq. S27. Supposing we wish to measure the correlator between qubits i and j , we apply the following rotation to the state Ψ :

$$|\Psi\rangle \rightarrow |\Psi_{R(\varphi)}\rangle = V_i(0)V_j(\varphi)|\Psi\rangle \quad (\text{S28})$$

where V is a three-part rotation in the 01, 12, and 01 qubit subspaces:

$$V_i(\varphi) = U_{i,\alpha}^{01}(\varphi)U_{i,\beta}^{12}(\varphi)U_{i,\gamma}^{01}(\varphi) \quad (\text{S29})$$

with

$$U_{i,\alpha}^{ab}(\varphi) = \exp \left\{ -i \frac{\alpha}{2} (e^{i\varphi} X_{ab} + e^{-i\varphi} X_{ba}) \right\}; \quad X_{ab} = |a\rangle\langle b|; \quad a, b \in \{0, 1, 2\} \quad (\text{S30})$$

The specific values of the angles we choose are:

$$\begin{aligned} \alpha &= \pi/2 \\ \beta &= 2 \arccos \left(\frac{1}{\sqrt{3}} \right) \\ \gamma &= \pi/3 \end{aligned} \quad (\text{S31})$$

One can show that

$$V_i^\dagger(\varphi)(n_i - 1)V_i(\varphi) = \frac{1}{\sqrt{3}} (e^{i\varphi} a_i + e^{-i\varphi} a_i^\dagger) \quad (\text{S32})$$

Using this fact, we obtain

$$\langle \Psi_{R(\varphi)} | (n_i - 1)(n_j - 1) | \Psi_{R(\varphi)} \rangle = \frac{1}{3} \langle \Psi | (a_i + a_i^\dagger) (e^{i\varphi} a_j + e^{-i\varphi} a_j^\dagger) | \Psi \rangle \quad (\text{S33})$$

If $|\Psi\rangle$ is number-conserving, then

$$\langle \Psi | a_i a_j | \Psi \rangle = \langle \Psi | a_i^\dagger a_j^\dagger | \Psi \rangle = 0, \quad (\text{S34})$$

and we parameterize the correlator as $\langle \Psi | a_i^\dagger a_j | \Psi \rangle = C_{ij} e^{i\phi_{ij}}$, then we are left with our expression for the correlator, Eq. S27.

C. Accounting for phase offset

Allow us to define the frame in which measurements are performed and microwave pulses applied as the ‘measurement frame’. We know from Ramsey experiments that if the qubits are prepared in the state $\frac{1}{\sqrt{2}}(|0\rangle + |2\rangle)$, the relative phase in that state does not evolve over time in this frame, assuming the anharmonicity is well calibrated in the registry. To arrive at a system of interacting bosons, we must put the qubits (originally at their ‘idle’ frequencies) on resonance. We call the corresponding frame the ‘interaction frame’. In this frame, the Hamiltonian is

approximately

$$\frac{H_I}{2\pi} = -g(t) \sum_{\langle i,j \rangle} a_i^\dagger a_j - \sum_i \frac{\eta_i}{2} n_i (n_i - 1) + \sum_i (f_{\text{idle}}(t) - f_{\text{int},i}) n_i, \quad (\text{S35})$$

To transform between the frames, we need to rotate by

$$\frac{H_0}{2\pi} = \sum_i \frac{\eta_i}{2} n_i (n_i - 1) + \sum_i (f_{\text{int},i} - f_{0,i}) n_i, \quad (\text{S36})$$

where f_0 is the idle frequency. Let the state, considered in the interaction frame, be $|\psi_I(t)\rangle$. Suppose, at time t_0 , we instantly turn off the coupling, g and bring the qubits to their idle frequencies, $f_{0,i}$. Then the quantity that we would like to measure can be written in the interaction picture as

$$C_{ij}^{(1)} e^{-i\chi^{(1)}} = \langle \psi_I(t_0) | a_i^\dagger a_j | \psi_I(t_0) \rangle. \quad (\text{S37})$$

However, we measure in the measurement frame, in which the state is $|\psi_M(t)\rangle$. Therefore, what we measure instead is $\langle \psi_M(t) | a_i^\dagger a_j | \psi_M(t) \rangle$. For $t > t_0$, when $g = 0$, this is given by

$$\begin{aligned} \langle \psi_M(t) | a_i^\dagger a_j | \psi_M(t) \rangle &= \langle \psi_I(t) | e^{iH_0 t} a_i^\dagger a_j e^{-iH_0 t} | \psi_I(t) \rangle \\ &= \langle \psi_I(t_0) | e^{iH_I(t-t_0)} e^{iH_0 t} a_i^\dagger a_j e^{-iH_0 t} e^{-iH_I(t-t_0)} | \psi_I(t_0) \rangle \\ &= \langle \psi_I(t_0) | e^{iH_0 t_0} a_i^\dagger a_j e^{-iH_0 t_0} | \psi_I(t_0) \rangle, \end{aligned} \quad (\text{S38})$$

where we have used the fact that, for $t > t_0$, $H_I = -H_0$. This shows that, in fact, we expect oscillations as a function of t_0 rather than t . Note that, in the last equation, H_I is evaluated with $g = 0$ and $f_i = f_{0,i}$. We can see how the measured quantity oscillates with t_0 by evaluating:

$$e^{iH_0 t_0} a_i^\dagger a_j e^{-iH_0 t_0} = e^{-2\pi i(f_{0,i} - f_{0,j})t_0} \left(|10\rangle\langle 01| + \sqrt{2}e^{2\pi i\eta_i t_0} |20\rangle\langle 11| + \sqrt{2}e^{-2\pi i\eta_j t_0} |11\rangle\langle 02| + 2e^{2\pi i(\eta_i - \eta_j)t_0} |21\rangle\langle 12| \right). \quad (\text{S39})$$

Thus, we see that the overall phase oscillates at the difference between the idle frequencies, and that relative phases oscillate at η_i , η_j and $\eta_i - \eta_j$. One workable protocol, therefore, is to measure the correlator as a function of t_0 (for example, by sweeping the hold time), and extract the coefficients, $\rho_{01,10}$, $\rho_{11,20}$, $\rho_{20,11}$, and $\rho_{12,21}$.

Equation S38 can be easily generalized. It did also not depend on the coupling being turned off instantly. More generally, for an operator \mathcal{O} , it becomes

$$\langle \psi_M(t) | \mathcal{O} | \psi_M(t) \rangle = \langle \psi_I(t_0) | e^{iH_0 t_0} \mathcal{O} e^{-iH_0 t_0} | \psi_I(t_0) \rangle, \quad (\text{S40})$$

for any times t and t_0 such that, for all $t' \geq \min(t, t_0)$, $g(t') = 0$ and $f_i(t') = f_{0,i}$. It follows trivially that

$$\langle \psi_M(t) | e^{-iH_0 t_0} \mathcal{O} e^{iH_0 t_0} | \psi_M(t) \rangle = \langle \psi_I(t_0) | \mathcal{O} | \psi_I(t_0) \rangle. \quad (\text{S41})$$

The RHS of Equation S41 is the quantity of interest, and the LHS can be obtained experimentally. In particular, we take the operator that we want to measure, evolve it forward in time under H_0 by amount t_0 , and measure it in the state $|\psi_M(t)\rangle$.

In our protocol for measuring the correlator, we consider the case

$$\mathcal{O} = \left(U_\gamma^\dagger U_\beta^\dagger U_\alpha^\dagger n U_\alpha U_\beta U_\gamma \right)_i (\varphi) \otimes \left(U_\gamma^\dagger U_\beta^\dagger U_\alpha^\dagger n U_\alpha U_\beta U_\gamma \right)_j (\varphi + \delta). \quad (\text{S42})$$

Then, to evaluate $e^{-iH_0 t_0} \mathcal{O} e^{iH_0 t_0}$, since H_0 is a sum over single-qubit terms and is diagonal, we need only consider

$$e^{-iH_0 t_0} U_\gamma^\dagger U_\beta^\dagger U_\alpha^\dagger n U_\alpha U_\beta U_\gamma e^{iH_0 t_0} = e^{-iH_0 t_0} U_\gamma^\dagger U_\beta^\dagger U_\alpha^\dagger n e^{-iH_0 t_0} U_\alpha U_\beta U_\gamma e^{iH_0 t_0}, \quad (\text{S43})$$

and further,

$$e^{-iH_0 t_0} U_\alpha U_\beta U_\gamma e^{iH_0 t_0} = e^{-iH_0 t_0} U_\alpha e^{iH_0 t_0} e^{-iH_0 t_0} U_\beta e^{iH_0 t_0} e^{-iH_0 t_0} U_\gamma e^{iH_0 t_0}, \quad (\text{S44})$$

so it is sufficient to evolve each $U_{\alpha(\beta,\gamma)}$ under H_0 by amount t_0 .

Because

$$\begin{aligned} U_\alpha &= \cos \alpha |0\rangle\langle 0| - ie^{i\varphi} \sin \alpha |0\rangle\langle 1| - ie^{-i\varphi} \sin \alpha |1\rangle\langle 0| + \cos \alpha |1\rangle\langle 1| \\ U_\beta &= \cos \beta |1\rangle\langle 1| - ie^{i\varphi} \sin \beta |1\rangle\langle 2| - ie^{-i\varphi} \sin \beta |2\rangle\langle 1| + \cos \beta |2\rangle\langle 2| \\ U_\gamma &= \cos \gamma |0\rangle\langle 0| - ie^{i\varphi} \sin \gamma |0\rangle\langle 1| - ie^{-i\varphi} \sin \gamma |1\rangle\langle 0| + \cos \gamma |1\rangle\langle 1| \end{aligned} \quad (\text{S45})$$

it follows that

$$\begin{aligned} e^{-iH_0 t_0} U_{\alpha,i}(\varphi) e^{iH_0 t_0} &= U_{\alpha,i}(\varphi + 2\pi(f_{\text{int},i} - f_{0,i})t_0) \\ e^{-iH_0 t_0} U_{\beta,i}(\varphi) e^{iH_0 t_0} &= U_{\beta,i}(\varphi + 2\pi(f_{\text{int},i} - f_{0,i} + \eta_i)t_0) \\ e^{-iH_0 t_0} U_{\gamma,i}(\varphi) e^{iH_0 t_0} &= U_{\gamma,i}(\varphi + 2\pi(f_{\text{int},i} - f_{0,i})t_0) \end{aligned} \quad (\text{S46})$$

The implication is that to measure the correlator in the interaction frame at time t_0 , we perform the correlator tomography protocol in the measurement frame, except using $U_{\alpha(\gamma),i}(\varphi + 2\pi(f_{\text{int},i} - f_{0,i})t_0)$ instead of $U_{\alpha(\gamma),i}(\varphi)$ and $U_{\beta,i}(\varphi + 2\pi(f_{\text{int},i} - f_{0,i} + \eta_i)t_0)$ instead of $U_{\beta,i}(\varphi)$. Because we sweep over φ en route to arriving at a final expression for the correlator, we can define $\tilde{\varphi} = \varphi + 2\pi(f_{\text{int},i} - f_{0,i})t_0$ and then drop the tilde. We see now that the gates we should apply to qutrits i and j are

$$V_i \otimes V_j, \quad (\text{S47})$$

where

$$V_i = U_{\alpha,i}(\varphi) U_{\beta,i}(\varphi + 2\pi\eta_i t_0) U_{\gamma,i}(\varphi) \quad (\text{S48})$$

and

$$V_j = U_{\alpha,j}(\varphi + \delta + 2\pi(f_{0,i} - f_{0,j})t_0) U_{\beta,j}(\varphi + \delta + 2\pi(f_{0,i} - f_{0,j} + \eta_j)t_0) U_{\gamma,j}(\varphi + \delta + 2\pi(f_{0,i} - f_{0,j})t_0) \quad (\text{S49})$$

In particular, we can now use this protocol to measure the correlator in the interaction frame as a function of t_0 , for all t_0 after g is turned off. Once g is off, the Hamiltonian in the interaction frame is $-H_0$, so the correlator will oscillate exactly as in Eq. S39. We can fit this as a function of t_0 and infer its value without the unwanted phases.

D. Benchmarking

In order to validate our protocol for measuring correlators, $\langle a_i^\dagger a_j \rangle$, prepare the following state using a native fSim gate [58] and π pulses in the 01 and 12 subspaces:

$$\begin{aligned} |\psi\rangle &= X_{01}^{(0)} X_{12}^{(0)} \text{fSim}(\theta, \phi) X_{01}^{(0)} |00\rangle \\ &= X_{01}^{(0)} X_{12}^{(0)} \text{fSim}(\theta, \phi) |01\rangle \\ &= X_{01}^{(0)} X_{12}^{(0)} (\cos \theta |01\rangle - i \sin \theta |10\rangle) \\ &= X_{01}^{(0)} (\cos \theta |02\rangle - i \sin \theta |10\rangle) \\ &= \cos \theta |02\rangle - i \sin \theta |11\rangle \end{aligned} \quad (\text{S50})$$

in which the correlator has the expectation value

$$\begin{aligned} C_{01} &= \langle \psi | a_1^\dagger a_0 | \psi \rangle \\ &= (\cos \theta \langle 02 | + i \sin \theta \langle 11 |) (\sqrt{2} \cos \theta |11\rangle - i \sqrt{2} \sin \theta |20\rangle) \\ &= i \sqrt{2} \sin \theta \cos \theta \\ &= \frac{i}{\sqrt{2}} \sin(2\theta). \end{aligned} \quad (\text{S51})$$

We implement the fSim gate for several θ values by turning on the the coupling between the two qubits for a fixed duration at several different coupling strengths. The qubits are at the same frequency during this gate. Using unitary tomography, we characterize the angle θ for each coupling strength. The θ angle is approximately proportional to the coupling strength. Using these characterized gates, we now prepare the state $|\psi\rangle$ (Eq. S50) and measure the correlators using our protocol. We compare the measured correlators to those predicted from Eq. S51 for the characterized angle θ .

VII. Dynamical structure factor

A. Definition

Suppose we modulate the on-site qubit frequencies in a time- and position-dependent way. We think of this as applying an external potential that couples to the density of excitations, introducing the following term to the Hamiltonian:

$$H' = \sum_{\mathbf{r}} n(\mathbf{r}) \phi_{\text{ext}}(\mathbf{r}, t) \quad (\text{S52})$$

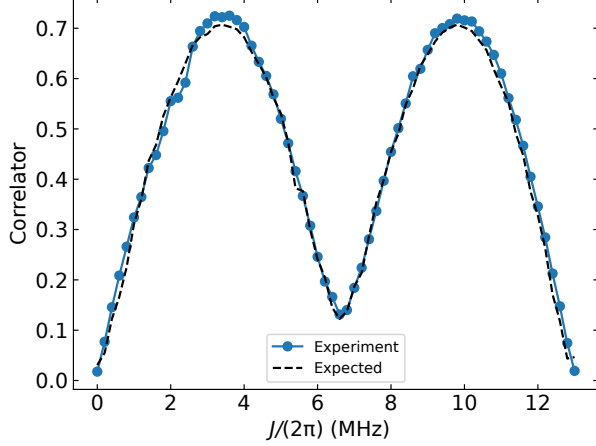


FIG. S4. **Benchmarking using the fSim gate.** Along the horizontal axis we show the inferred coupling strength J , while along the vertical axis we plot the value of the correlator. We compare data (blue) to the predicted theoretical value (dashed black line)

The induced density response follows from linear response theory, assuming $t > t'$:

$$\delta n(\mathbf{r}, t) = \sum_{\mathbf{r}'} \int_{t_0}^{\infty} dt' \chi^R(\mathbf{r}, t; \mathbf{r}', t') e^{-\eta(t-t')} \phi_{\text{ext}}(\mathbf{r}', t') \quad (\text{S53})$$

(We introduce the artificial relaxation mechanism $e^{-\eta(t-t')}$ to pick out the physically-relevant solution; at the end of the calculation, we take $\eta \rightarrow 0^+$). The polarizability (also known as the dynamical structure factor) χ^R is identified as the density-density correlation function by standard linear response theory:

$$\chi^R(\mathbf{r}, t; \mathbf{r}', t') = -i\Theta(t-t') \langle [n(\mathbf{r}, t), n(\mathbf{r}', t')] \rangle_0, \quad (\text{S54})$$

where the notation $\langle \dots \rangle_0$ indicates an expectation value taken with respect to the equilibrium state. In the presence of translational invariance, the polarizability can only depend on differences of the arguments, and therefore the problem is simplified by going to frequency and momentum space, where the expression above now takes the form of a convolution:

$$\delta n(\mathbf{k}, \omega) = \chi^R(\mathbf{k}, \omega) \phi_{\text{ext}}(\mathbf{k}, \omega) \quad (\text{S55})$$

Because the poles of the dynamical structure factor coincide with those of the interacting Green's function, one can use a measurement of this quantity to infer the spectrum. This remarkable property of interacting Bose systems stems from the condensate-induced intermixing of single-particle and density excitations; for a full derivation, see Ref. [40].

B. Feynman-Bijl Ansatz

In this section we will introduce the Feynman-Bijl ansatz, originally applied to liquid helium, and generalize it to the case with broken translational symmetry. We will use this ansatz to make predictions about the dynamical structure factor measurement described above. We begin with the translationally-invariant case, where the ansatz [59] is

$$|k\rangle = A_k \int d\vec{r} e^{i\vec{k}\cdot\vec{r}} \hat{n}(\vec{r}) |GS\rangle \quad (\text{S56})$$

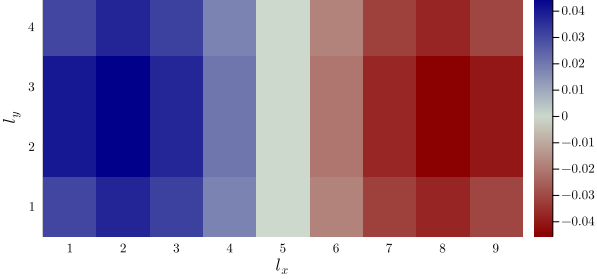
$$= A_k \hat{n}_k |GS\rangle \quad (\text{S57})$$

The operator \hat{n}_k is identified as the Fourier transform of the density,

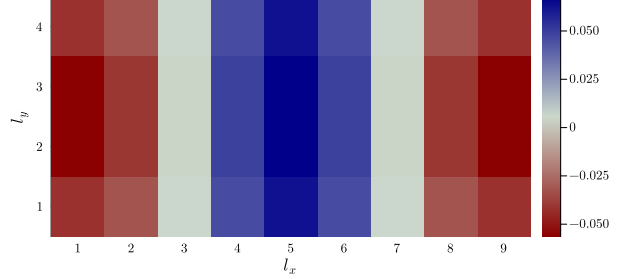
$$\hat{n}_k = \int d\vec{r} e^{i\vec{k}\cdot\vec{r}} \hat{n}(\vec{r}) \quad (\text{S58})$$

$$= \sum_q \hat{a}_{k+q}^\dagger \hat{a}_q \quad (\text{S59})$$

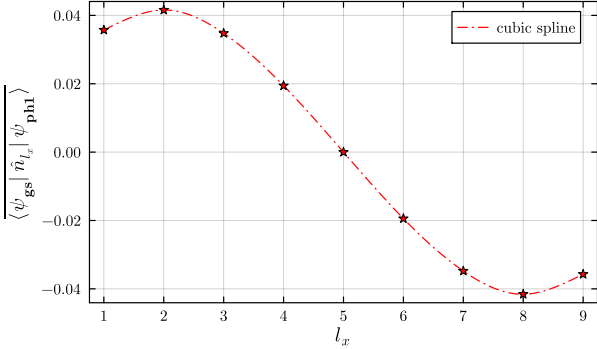
$$= V \int \frac{d^d q}{(2\pi)^d} \hat{a}_{k+q}^\dagger \hat{a}_q, \quad (\text{S60})$$



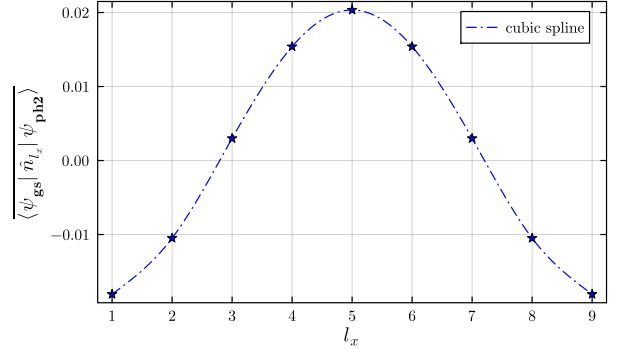
(a) Matrix elements of the density operator $\hat{n}_{(l_x, l_y)}$ between the ground state and the first goldstone mode for all sites.



(b) Matrix elements of the density operator $\hat{n}_{(l_x, l_y)}$ between the ground state and the second goldstone mode for all sites.



(c) Average x-slice shape of the profile from Fig. S5a.



(d) Average x-slice shape of the profile from Fig. S5b.

FIG. S5. Figure shows the sitewise matrix element profiles between the ground state and phonon/goldstone modes for the 4x9 Lattice using the Ideal Bose-Hubbard Model with $g = 20$ MHz and $\eta = 190$ MHz

As in earlier sections, V is the volume of the system. The state $|k\rangle$ is an eigenstate of the translation operator, and therefore represents a state with definite momentum. The normalization A_k is related to the static structure factor,

$$\langle k|k\rangle = A_k^2 \langle \hat{n}_{-k} \hat{n}_k \rangle \quad (\text{S61})$$

$$= A_k^2 N S_k, \quad (\text{S62})$$

which defines

$$S_k = \frac{1}{N} \langle \hat{n}_{-k} \hat{n}_k \rangle. \quad (\text{S63})$$

Here N is the number of particles. Thus

$$A_k^2 = \frac{1}{N S_k}. \quad (\text{S64})$$

We now consider a generic Hamiltonian of the form

$$H = \sum_k \epsilon_k \hat{a}_k^\dagger \hat{a}_k + \frac{1}{2} \int d\vec{r} d\vec{r}' U(\vec{r} - \vec{r}') \hat{n}(\vec{r}) \hat{n}(\vec{r}'). \quad (\text{S65})$$

A variational upper bound on the energy, E_k , of an excitation with momentum k can be derived from the Feynman-Bijl ansatz accordingly:

$$E_k \leq E_k^{\text{FB}} \quad (\text{S66})$$

$$\equiv \langle k|H|k\rangle - E_0, \quad (\text{S67})$$

where ‘FB’ stands for ‘Feynman-Bijl’ and E_0 is the ground state energy. To calculate E_k^{FB} , we note that

$$H|k\rangle = H A_k \hat{n}_k |GS\rangle \quad (\text{S68})$$

$$= A_k [H, n_k] |GS\rangle + A_k n_k H |GS\rangle \quad (\text{S69})$$

$$= A_k [H, n_k] |GS\rangle + E_0 |k\rangle, \quad (\text{S70})$$

We then observe that n_k commutes with the interaction part of the Hamiltonian, so

$$[H, n_k] = \left[\sum_p \epsilon_p a_p^\dagger a_p, \sum_q a_{k+q}^\dagger a_q \right] \quad (\text{S71})$$

$$= \sum_q (\epsilon_{k+q} - \epsilon_q) a_{k+q}^\dagger a_q. \quad (\text{S72})$$

We can then calculate

$$E_k^{\text{FB}} = \langle k | H | k \rangle - E_0 \quad (\text{S73})$$

$$= A_k^2 \langle GS | n_{-k} [H, n_k] | GS \rangle \quad (\text{S74})$$

$$= A_k^2 \sum_{q,p} (\epsilon_{k+q} - \epsilon_q) \langle a_p^\dagger a_{p+k} a_{q+k}^\dagger a_q \rangle. \quad (\text{S75})$$

We then normal-order the expectation value,

$$E_k^{\text{FB}} = A_k^2 \sum_{q,p} (\epsilon_{k+q} - \epsilon_q) \left[\delta_{pq} \langle a_q^\dagger a_q \rangle + \langle a_p^\dagger a_{q+k}^\dagger a_{p+k} a_q \rangle \right] \quad (\text{S76})$$

The first term is

$$I = \sum_{q,p} (\epsilon_{k+q} - \epsilon_q) \delta_{pq} \langle a_q^\dagger a_q \rangle \quad (\text{S77})$$

$$= \sum_q n_q (\epsilon_{k+q} - \epsilon_q). \quad (\text{S78})$$

For He-4 one assumes a free-particle dispersion, $\epsilon_k = k^2/2m$, in which case

$$I = \sum_q \left(\frac{k^2}{2m} - \frac{k \cdot q}{m} \right) n_q \quad (\text{S79})$$

$$= N \frac{k^2}{2m} \quad (\text{S80})$$

where N is the total number of particles, and we have used that n_q is even in q . In our case we are on a lattice, so $\epsilon_k = -2t \cos(k_x) - 2t \cos(k_y)$, and so

$$I = \sum_q n_q (\epsilon_{k+q} - \epsilon_q) \quad (\text{S81})$$

$$= 2t(1 - \cos(k_x)) \sum_q n_q \cos q_x + 2t(1 - \cos(k_y)) \sum_q n_q \cos q_y \quad (\text{S82})$$

Again, we used the fact that n_q is even. We then note that the kinetic energy is (assuming C_4 symmetry)

$$T = \sum_q n_q \epsilon_q \quad (\text{S83})$$

$$= -2t \sum_q n_q (\cos q_x + \cos q_y) \quad (\text{S84})$$

$$= -4t \sum_q n_q \cos q_x = -4t \sum_q n_q \cos q_y \quad (\text{S85})$$

Thus on the square lattice, the quantity

$$I = \left(\frac{\cos k_x + \cos k_y}{2} - 1 \right) T \quad (\text{S86})$$

is just related to the average kinetic energy. Furthermore, the second term in Eq. (S76) vanishes. To show this, we define

$$J = \sum_{q,p} (\epsilon_{k+q} - \epsilon_q) \langle a_p^\dagger a_{q+k}^\dagger a_{p+k} a_q \rangle \quad (\text{S87})$$

$$= \sum_{q,p} \epsilon_q \left[\langle a_p^\dagger a_q^\dagger a_{p+k} a_{q-k} \rangle - \langle a_p^\dagger a_{q+k}^\dagger a_{p+k} a_q \rangle \right] \quad (\text{S88})$$

We use that p is a dummy variable, and shift it in the first term, $p \rightarrow -p - k$ so

$$J = \sum_{q,p} \epsilon_q \left[\langle a_{-p-k}^\dagger a_q^\dagger a_{-p} a_{q-k} \rangle - \langle a_p^\dagger a_{q+k}^\dagger a_{p+k} a_q \rangle \right] \quad (\text{S89})$$

Next we use that ϵ_q is even, and in the first term take $q \rightarrow -q$, so

$$J = \sum_{q,p} \epsilon_q \left[\langle a_{-p-k}^\dagger a_{-q}^\dagger a_{-p} a_{-q-k} \rangle - \langle a_p^\dagger a_{q+k}^\dagger a_{p+k} a_q \rangle \right]. \quad (\text{S90})$$

We finally note that the two terms in the square bracket must be equal to one-another, since the ground state is inversion symmetric. As a result, we conclude that

$$E_k^{\text{FB}} = A_k^2 \sum_q n_q (\epsilon_{k+q} - \epsilon_q) \quad (\text{S91})$$

$$\rightarrow \frac{k^2}{2mS_k} \quad (\text{free space}) \quad (\text{S92})$$

$$\rightarrow \frac{T}{N} \frac{\cos k_x + \cos k_y - 2}{2S_k} \quad (\text{square lattice}) \quad (\text{S93})$$

Feynman then argues that S_k is linear at long wavelengths, which means that $E_k^{\text{FB}} \propto k$ in this regime. The linear dispersion is identified with phonons.

C. Inhomogeneous system

Let us now generalize the Feynman-Bijl ansatz to the inhomogeneous case. In the absence of translational symmetry, the excited states are given by

$$|\phi\rangle = \sum_j \phi_j \hat{n}_j |GS\rangle, \quad (\text{S94})$$

where ϕ_j describes the shape of mode j . By the variational principle, this ansatz should make the Hamiltonian stationary:

$$\frac{\partial}{\partial \phi_j^*} [\langle \phi | (H - E_0) | \phi \rangle - \lambda \langle \phi | \phi \rangle] = 0, \quad (\text{S95})$$

In the expression above, λ is a Lagrange multiplier that enforces normalization of the wavefunction; at the stationary point, it is equal to $E - E_0$. The excited states must be orthogonal, so

$$\langle \psi | \phi \rangle = \sum_{ij} \psi_i^* \phi_j \langle GS | n_i n_j | GS \rangle = 0. \quad (\text{S96})$$

To calculate $\langle \phi | H | \phi \rangle$, we use a trick similar to that employed in the homogeneous case. We first define the density operator

$$\hat{\rho}_\phi = \sum_j \phi_j \hat{n}_j. \quad (\text{S97})$$

We can then write

$$H|\phi\rangle = H\hat{\rho}_\phi|GS\rangle \quad (\text{S98})$$

$$= [H, \hat{\rho}_\phi]|GS\rangle + \rho_\phi H|GS\rangle \quad (\text{S99})$$

$$= [H, \hat{\rho}_\phi]|GS\rangle + E_0|\phi\rangle. \quad (\text{S100})$$

Again, the only part of the Hamiltonian which does not commute with $\hat{\rho}_\phi$ is the kinetic term, which we write as

$$T = \sum_{ij} g_{ij} a_i^\dagger a_j. \quad (\text{S101})$$

We then have

$$[T, \rho_\phi] = \left[\sum_{ij} g_{ij} a_i^\dagger a_j, \sum_l \phi_l a_l^\dagger a_l \right] \quad (\text{S102})$$

$$= \sum_{ij} g_{ij} (\phi_j - \phi_i) a_i^\dagger a_j. \quad (\text{S103})$$

This then lets us write

$$\langle \phi | H - E_0 | \phi \rangle = \langle \rho_\phi^\dagger [T, \rho_\phi] \rangle \quad (\text{S104})$$

$$= \sum_{lij} \phi_l^* g_{ij} (\phi_j - \phi_i) \langle a_l^\dagger a_l a_i^\dagger a_j \rangle. \quad (\text{S105})$$

As before we normal order the operator, writing

$$\langle a_l^\dagger a_l a_i^\dagger a_j \rangle = \delta_{il} \langle a_i^\dagger a_j \rangle + \langle a_l^\dagger a_i^\dagger a_j a_l \rangle. \quad (\text{S106})$$

The contribution due to the second term vanishes as

$$J_l = \sum_{ij} g_{ij} (\phi_j - \phi_i) \langle a_l^\dagger a_i^\dagger a_j a_l \rangle \quad (\text{S107})$$

$$= \sum_{ij} g_{ij} \phi_j (\langle a_l^\dagger a_i^\dagger a_j a_l \rangle - \langle a_l^\dagger a_j^\dagger a_i a_l \rangle) \quad (\text{S108})$$

where we used $g_{ij} = g_{ji}$. The term in parentheses then vanishes due to time reversal symmetry. As a consequence

$$\langle \phi | H - E_0 | \phi \rangle = \sum_{ij} g_{ij} \phi_i^* (\phi_j - \phi_i) \langle a_i^\dagger a_j \rangle. \quad (\text{S109})$$

We then want to make stationary

$$\mathcal{L} = \langle \phi | H - E_0 | \phi \rangle - \lambda \langle \phi | \phi \rangle \quad (\text{S110})$$

$$= \sum_{ij} \phi_j^* \left[g_{ij} \langle a_i^\dagger a_j \rangle (\phi_j - \phi_i) - \lambda \langle n_i n_j \rangle \phi_j \right] \quad (\text{S111})$$

This means that the ϕ 's obey the generalized eigenvalue problem

$$\sum_j g_{ij} \langle a_i^\dagger a_j \rangle (\phi_j - \phi_i) = \lambda \sum_j \langle n_i n_j \rangle \phi_j. \quad (\text{S112})$$

We emphasize that the expectation values $\langle \dots \rangle$ are all taken with respect to the ground state, $|GS\rangle$. This illustrates how the dynamical properties of a superfluid can be inferred from its ground state characteristics. The difference between the insulator and the superfluid phase is captured in the matrix $\langle n_i n_j \rangle$. In the insulating phase the density fluctuations are all short ranged, while in the superfluid they are long-ranged.

The solutions of this equation automatically obey the orthogonality relationship in Eq. (S96) as long as they each correspond to a different λ . Recall that the eigenvalue λ is simply the excitation energy. We immediately find one solution $\phi_j = \text{const.}$, with $\lambda = 0$. This is simply the ground state itself. In the special case of translational invariance, the solutions are plane waves, and we recover our uniform results. Specifically, in a homogeneous system one assumes that $\langle n_i n_j \rangle$ and $a_i^\dagger a_j$ are only functions of $i - j$. In that case we can take $\phi_i = e^{ik \cdot r_i}$, and we get

$$\lambda = E - E_0 \quad (\text{S113})$$

$$= \frac{\sum_j g_{ij} \langle a_i^\dagger a_j \rangle (e^{ik \cdot (r_j - r_i)} - 1)}{\sum_j \langle n_i n_j \rangle e^{ik \cdot (r_j - r_i)}}, \quad (\text{S114})$$

which is easily seen to be equivalent to Eq. (S93).

D. Calculating the dynamical structure factor with Feynman-Bijl ansatz

Let us consider a Bose-Hubbard Hamiltonian H_0 under a time-dependent perturbation:

$$\hat{H} = \hat{H}_0 + \cos(\omega_d t + \varphi) \delta \hat{H}, \quad (\text{S115})$$

where

$$\delta \hat{H} = \Delta \sum_i \gamma_i \hat{n}_i \quad (\text{S116})$$

is a non-uniform spatial part of the perturbation. Using time-dependent perturbation theory at $T = 0$ one can express density perturbation on site i as:

$$\langle \delta n_i(t) \rangle = \sum_{m \neq 0} \langle 0 | \hat{n}_i | m \rangle \langle m | \delta \hat{H} | 0 \rangle \chi_m(t), \quad (\text{S117})$$

where

$$\chi_m(t) = \text{Re} \left(\frac{e^{i(\omega_d t + \varphi)}}{\omega_d + i\eta - \omega_{m0}} - \frac{e^{-i(\omega_d t + \varphi)}}{\omega_d + i\eta + \omega_{m0}} \right), \quad (\text{S118})$$

In the expression above, we define $\omega_{m0} = \omega_m - \omega_0$. To get the retarded part, we take $\eta \rightarrow +0$. We now use the generalized Feynman-Bijl ansatz for the excited states $|m\rangle$ of H_0 :

$$|m\rangle = \sum_j \phi_j^{(m)} \hat{n}_j |0\rangle, \quad (\text{S119})$$

set $\gamma_i = \phi_i^{(l)}$ in Eq. (S116) and project Eq. (S117) onto an eigenmode $|k\rangle$. This yields:

$$\sum_i \phi_i^{(k)} \langle \delta n_i(t) \rangle = \Delta \cdot \chi_k(t) \delta_{kl} \quad (\text{S120})$$

In other words, the polarizability is found by driving the system at its fundamental modes.

In the vicinity of the k_{th} resonance we have to solve the Schrödinger equation for a two-level Hamiltonian involving states $|0\rangle$ and $|k\rangle$ non-perturbatively. The effective Hamiltonian in the rotating wave approximation (RWA) reads:

$$H = \begin{pmatrix} -i(\gamma_s - \gamma)/2 & \frac{1}{2}\Delta e^{-i\omega_d t} \\ \frac{1}{2}\Delta e^{i\omega_d t} & \omega_{k0} - i(\gamma_s + \gamma)/2 \end{pmatrix} \quad (\text{S121})$$

Here $\gamma_0 = (\gamma_s - \gamma)/2$, $\gamma_k = (\gamma_s + \gamma)/2$ are the T_1 decay rates of the state $|0\rangle$ and $|k\rangle$ respectively. The parameter γ describes asymmetry in the T_1 decay caused by the spread of T_1 times for different qutrits. While the average decay γ_s can be remedied using post-selection on the total number of particles, the T_1 asymmetry depends on the spatial character of the wave function and must be taken into account explicitly.

The solution of the Schrödinger equation can be readily found:

$$c_0(t) = e^{-\gamma_s t/2} e^{i\omega_d t/2} \left(\frac{(\gamma + i\epsilon) \sin\left(\frac{1}{2}(\alpha + i\Gamma)t\right)}{\alpha + i\Gamma} + \cos\left(\frac{1}{2}(\alpha + i\Gamma)t\right) \right) \quad (\text{S122})$$

$$c_k(t) = -ie^{-\gamma_s t/2} e^{-i\omega_d t/2} \frac{\Delta \sin\left(\frac{1}{2}(\alpha + i\Gamma)t\right)}{\alpha + i\Gamma}. \quad (\text{S123})$$

Here, the detuning $\epsilon = \omega_{k0} - \omega_d$, $\alpha = \Omega \cos(\theta)$ and $\Gamma = \Omega \sin(\theta)$ are the real and imaginary parts of the complex Rabi frequency, respectively, with

$$\Omega = \left((\Delta^2 + \epsilon^2 - \gamma^2)^2 + 4\gamma^2 \epsilon^2 \right)^{1/4} \quad \text{and} \quad \theta = -\frac{1}{2} \arctan \left(\frac{2\gamma\epsilon}{\Delta^2 + \epsilon^2 - \gamma^2} \right).$$

Using Eqs. (S122) and (S123) we can find susceptibility in Eq. (S120)

$$\chi_k(t) = \frac{\Delta \langle k | \hat{\nu}_k | k \rangle}{2\Omega^2 n(t)} (\cosh(\Gamma t) - \cos(\alpha t)) + \frac{1}{\Omega^2 n(t)} (\cos(\omega_d t) r_k(t) + \sin(\omega_d t) a_k(t)) \quad (\text{S124})$$

where $\hat{\nu}_k = \sum_i \phi_i^{(k)} \hat{n}_i$, and “in phase” and “in quadrature” envelopes are

$$r_k(t) = -\Gamma \sin(\alpha t) + \alpha \sinh(\Gamma t) + \epsilon \cos(\alpha t) - \epsilon \cosh(\Gamma t) \quad (\text{S125})$$

$$a_k(t) = -\gamma \cos(\alpha t) + \alpha \sin(\alpha t) + \gamma \cosh(\Gamma t) + \Gamma \sinh(\Gamma t) \quad (\text{S126})$$

The factor $n(t) = e^{\gamma_s t} (|c_0(t)|^2 + |c_k(t)|^2)$ appears because of the post selection. In the vicinity of the resonance

$$n(t) \simeq 1 + \frac{\gamma}{\alpha} \sin(\alpha t) + \frac{\gamma^2}{\alpha^2} \sin^2\left(\frac{\alpha t}{2}\right) \quad (\text{S127})$$

The system responds at different frequencies such as ω_d , α , $\omega_d \pm \alpha$ and higher harmonics. But there is always a robust feature in the Fourier spectrum of the susceptibility:

$$\text{Re}(\chi_k(\omega)) \propto \epsilon \cdot \delta(\omega - \omega_d) \quad (\text{S128})$$

This peak is present off resonance and disappears on resonance. Therefore we can detect the resonance by finding zeros of the real part of the susceptibility at the driving frequency. In Fig. S6, we plot the raw real and imaginary parts of the susceptibility for four different points in the phase diagram:

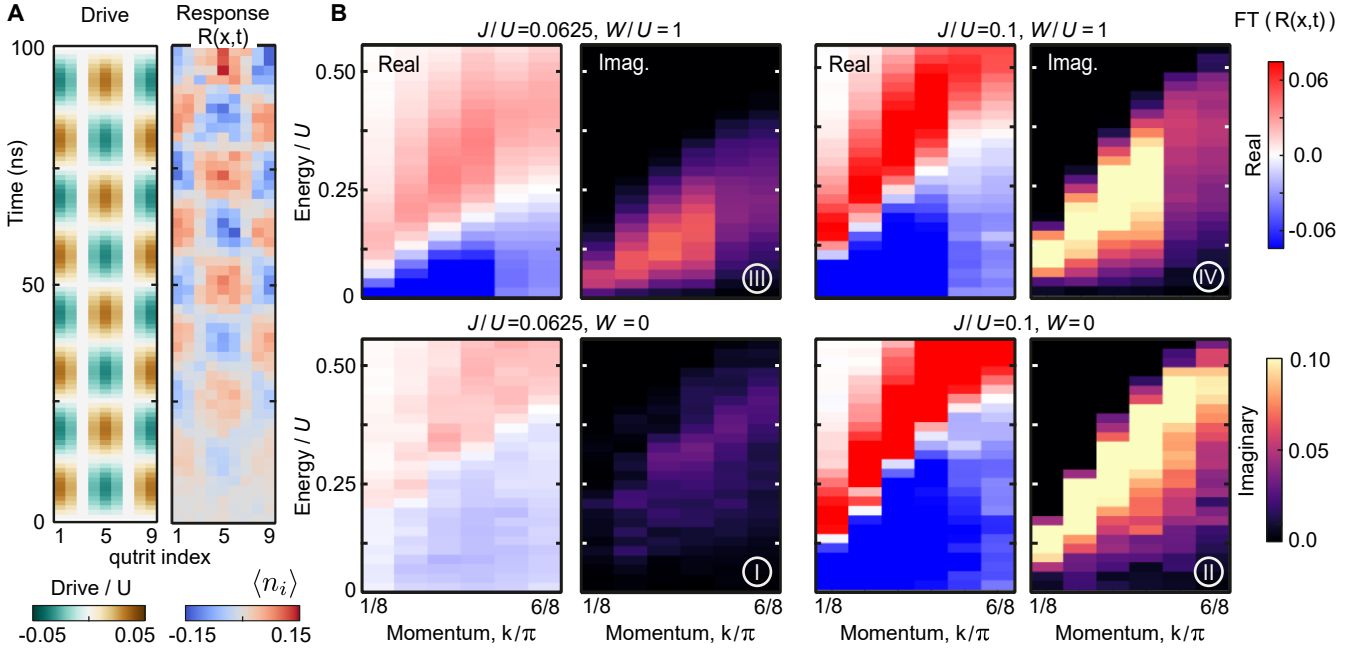


FIG. S6. **Dynamical structure factor.** (A) Typical drive (left) and response (right) with momentum $k = 2\pi/8$ and frequency $\omega/(2\pi) = 40$ MHz. (B) Real and imaginary parts of the susceptibility for four different points in the phase diagram

VIII. Calculating excitation spectrum using Gutzwiller ansatz

Here we briefly describe excitation spectrum of a lattice superfluid using the Gutzwiller ansatz for the Bose-Hubbard Hamiltonian, i.e. represent the eigenstates of the Hamiltonian as product states over lattice sites:

$$|\Psi\rangle = \prod_l \otimes \sum_n c_{l,n} |l, n\rangle, \quad (\text{S129})$$

where $|l, n\rangle$ is the local Fock state with n excitations on site l . Since we are interested in the long-wave excitations in the vicinity of the MI-SF transition we will consider a uniform system and a truncated version of the ansatz restricting the sum in Eq. (S129) to $|0\rangle$, $|1\rangle$ and $|2\rangle$ Fock states. As a first step, we start with the static mean-field Hamiltonian [60, 61]:

$$H_{\text{MF}} = \frac{\eta}{2} a^\dagger a (a^\dagger a - 1) - \mu a^\dagger a - g\psi(a^\dagger + a), \quad (\text{S130})$$

where a and a^\dagger are truncated annihilation and creation operators, μ is the chemical potential, $\psi = \frac{1}{2}\langle\chi_0|a^\dagger + a|\chi_0\rangle$ is the equilibrium superfluid order parameter and $|\chi_0\rangle$ is the ground state. Without any loss of generality we chose the equilibrium order parameter and the mean-field eigenstates to be real.

Since the original Hamiltonian is number conserving, $|\chi_0\rangle$ can be expressed as follows

$$|\chi_0\rangle = \cos(\varphi)|1\rangle + \frac{1}{\sqrt{2}}\sin(\varphi)(|0\rangle + |2\rangle) \quad (\text{S131})$$

Here φ is the variational parameter that minimizes the expectation value of the Hamiltonian. The minimization procedure is straightforward and allows us to find φ as:

$$\varphi = \frac{1}{2} \arccos(\alpha_c \eta / 4g) \equiv \frac{1}{2} \arccos(1/\gamma), \quad (\text{S132})$$

where $\alpha_c = 3 - 2\sqrt{2}$ is the mean-filed value of the critical point for MI-SF transition. Therefore the superfluid state emerges when $\gamma = 4g/\alpha_c \eta > 1$, i.e. parameter γ is a measure of the departure from the critical point to the superfluid phase.

Using Eq. (S132) we can find the equilibrium values of the chemical potential

$$\mu = \frac{\eta}{2} \left(1 - \alpha_c - \frac{\alpha_c}{2} (\gamma - 1) \right) \quad (\text{S133})$$

and the order parameter

$$\psi = \frac{1}{\sqrt{8\alpha_c}} \sqrt{1 - (1/\gamma)^2} \quad (\text{S134})$$

To find the excitation spectrum we use the method of Refs [62, 63] (see also [64, 65]). As shown in [63] we take into account quantum fluctuations around the mean-field solution by applying a small plane-wave perturbation to the time-dependent Gutzwiller equations and representing coefficients $c_{l,n}$ in Eq. (S129) in the form of plane waves:

$$c_{l,n}(t) = u_{kn} e^{i(\mathbf{kl} - \omega(\mathbf{k})t)} - v_{kn}^* e^{-i(\mathbf{kl} - \omega(\mathbf{k})t)} \quad (\text{S135})$$

This results in the eigenvalue problem for the effective non-Hermitian Hamiltonian H_{eff} :

$$\omega(\mathbf{k}) \begin{pmatrix} u_{\mathbf{k}} \\ v_{\mathbf{k}} \end{pmatrix} = H_{\text{eff}}(\mathbf{k}) \begin{pmatrix} u_{\mathbf{k}} \\ v_{\mathbf{k}} \end{pmatrix}, \quad (\text{S136})$$

where

$$H_{\text{eff}}(\mathbf{k}) = \sigma_z \otimes (H_{\text{mf}} - \omega_0 \mathbb{1}) - g (1 - \xi(\mathbf{k})) (\sigma_z \otimes X + i\sigma_y \otimes Y). \quad (\text{S137})$$

Here $\omega_0 = (\eta/2) (1 - \sqrt{2} - (1 + \sqrt{2})\alpha_c \gamma)$ is the ground state energy, $\mathbb{1}$ is the 3×3 unit matrix, σ_x and σ_y are the Pauli matrices, $\xi(\mathbf{k}) = \sin^2(k_x/2) + \sin^2(k_y/2)$ and

$$X = \chi_a \otimes \chi_a + \chi_c \otimes \chi_c \quad (\text{S138a})$$

$$Y = \chi_a \otimes \chi_c + \chi_c \otimes \chi_a \quad (\text{S138b})$$

where $\chi_c = (\cos(\varphi), \sin(\varphi), 0)$, and $\chi_a = (0, \sin(\varphi)/\sqrt{2}, \sqrt{2}\cos(\varphi))$ are the vectors comprised of the matrix elements $\langle n|a^\dagger|\chi_0\rangle$ and $\langle n|a|\chi_0\rangle$ respectively.

The eigenvalue problem (S136) can be solved using Bogoliubov transformation. The matrix $H_{\text{eff}}(\mathbf{k})$ in Eq. (S137) is non-diagonalizable and must be reduced to the Jordan form. After separating out two linearly dependent solutions corresponding to the condensate mode with $\omega = 0$, the remaining 4×4 matrix can be diagonalized using Bogoliubov transformation. There are two pairs of eigenvalues $\pm\omega(\mathbf{k})$ describing the excited states in question. The positive and negative solutions in each pair are equivalent and it is sufficient to consider only the positive eigenvalues. Thus the frequencies of the two excited states at a given \mathbf{k} take the form:

$$\omega_{\mp}(\mathbf{k}) = \frac{\eta}{4} \sqrt{A(\mathbf{k}) \mp \sqrt{A^2(\mathbf{k}) - B(\mathbf{k})}}, \quad (\text{S139})$$

where “-” stands for the lower (Goldstone) and “+” for the upper (Higgs) mode respectively. The functions $A(\mathbf{k})$ and $B(\mathbf{k})$ can be found analytically:

$$A(\mathbf{k}) = 8\alpha_c \xi(\mathbf{k}) (2\sqrt{2} + \alpha_c \xi(\mathbf{k})) + \frac{\alpha_c}{2} (\gamma - 1) (16\sqrt{2}(1 + \gamma) + 2(9 + \alpha_c + 3(1 + \alpha_c)\gamma) \xi(\mathbf{k}) + \alpha_c(7 + \gamma) \xi^2(\mathbf{k})), \quad (\text{S140a})$$

$$B(\mathbf{k}) = 16\alpha_c^2 \xi(\mathbf{k}) (\sqrt{2}\alpha_c (\gamma^2 - 1)^2 (\xi(\mathbf{k}) - 3) + 2(1 + \gamma)^2 (\sqrt{2}\alpha_c (\gamma - 1)^2 + 4(\xi(\mathbf{k}) + \gamma^2 - 1))), \quad (\text{S140b})$$

In the long-wavelength limit $\xi(\mathbf{k}) \simeq (k_x^2 + k_y^2)/4$ and the spectrum is isotropic. Using small k expansion of (S139) we can find the speed of sound

$$c_s = \frac{\eta}{4} \left(\sqrt{2}\alpha_c \right)^{1/2} (\gamma + 1) \left(1 - \frac{\alpha_c(\gamma - 1)}{4\sqrt{2}(\gamma + 1)} \right)^{1/2} \simeq \frac{\eta}{4} \left(\sqrt{2}\alpha_c \right)^{1/2} (\gamma + 1) \quad (\text{S141})$$

and the frequency of the Higgs mode:

$$\omega_H = \omega_+(0) = \eta \left(\sqrt{2}\alpha_c \right)^{1/2} \sqrt{\gamma^2 - 1} \quad (\text{S142})$$

It is interesting to note that the ratio of ω_H to c_s depends only on the parameter γ which describes the departure from the critical point:

$$\frac{\omega_H}{c_s} \simeq 4 \left(\frac{\gamma - 1}{\gamma + 1} \right)^{1/2} \quad (\text{S143})$$

The dispersion curves overlaid with the data are shown in Fig. 5 of the main text. Quite surprisingly, after rescaling α_c and γ to more realistic values such as $\alpha_c = 0.3$ and $\gamma = 1.1$, the dispersion curve for the Goldstone mode is remarkably close to the experiment.

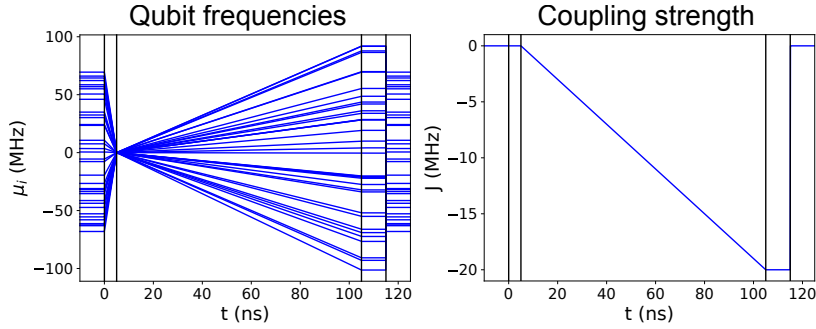


FIG. S7. Illustration of the adiabatic state preparation procedure for coupling strength $J/(2\pi) = 20$ MHz and disorder $W/(2\pi) = 200$ MHz, for one randomly chosen disorder realization. The left panel shows the chemical potentials of all qubits as a function of time; the right panel shows nearest-neighbor coupling strength. Until time $t = 0$ ns the system is at idle, with no coupling. (The true idle frequencies have been replaced with random values.) The qubits are brought onto resonance by $t = 5$ ns, then over 100 ns the coupling is adiabatically switched on and the qubit frequencies are ramped to their final disorder configuration. The system is held with this constant Hamiltonian for 10 ns, and then quickly ramped back to idle (here shown as a perfect instantaneous quench, though that is not possible in practice). Vertical black lines indicate where ramps begin and end.

IX. Matrix product state simulations

For comparison with the experimental results, we also performed large-scale matrix product state (MPS) [56, 66] simulations. We study the same system size used in the experiments, a 4×9 rectangular array of sites. To capture the physics of the Bose-Hubbard model at filling 1, we need to include at least three states per site, $|0\rangle$, $|1\rangle$, and $|2\rangle$, giving a total Hilbert space size of $3^{36} \approx 2^{57}$. Even when using particle number conservation, the Hilbert space size is larger than 2^{53} , beyond what is accessible via any exact state vector method, hence the use of tensor networks. We choose not to include the $|3\rangle$ and higher states on each site, as they are not needed to capture the physics of interest.

To gain insight into how well the experiment reproduces the ideal ground state phase diagram, we use a variety of approaches to simulating the system: we use both an idealized Bose Hubbard model and a device-accurate model with long-ranged and up to 3-body terms, and we use both direct ground state search and simulation of adiabatic state preparation. For concreteness in explaining these different approaches to the simulation, we illustrate an idealized adiabatic state preparation procedure (Sec. IV) in Fig. S7. Note that the initial and final chemical potentials (qubit frequencies) have been replaced with random values, but the frequencies after the ramp (i.e. the qubit frequencies for the Hamiltonian we want to study) are taken directly from one disorder realization in the experiment.

With each simulation type, we compute experimental observables such as doublon fraction and condensate fraction, as well as theoretical quantities such as entanglement entropy, throughout the J - W phase diagram.

A. Simulation types

We perform a variety of eigenstate and time evolution simulations to gain insight into our experiments, with the goal of understanding the extent to which the experimentally observed phase diagram is representative of the true ground state phase diagram, both qualitatively and quantitatively. The simulation approaches are as follows:

Ideal ground state: We first compute the ideal ground state phase diagram. For each coupling strength J and disorder strength W , we use the exact same disorder realizations studied in the experiment, using the density matrix renormalization group (DMRG) algorithm [54–56] to find the ground state of the Hamiltonian that is intended to be implemented after the ramp-up and before the ramp-down/quench in the adiabatic state preparation procedure; with times defined as in Fig. S7, the Hamiltonian is taken at $t = 110$ ns. This includes disorder in qubit frequencies (we use the same 10 disorder realizations as in the experiments), but does not include perturbative long-ranged interactions or higher-than-2-body terms present in the experiment.

We perform the simulations with a fixed max bond dimension χ , and we observe convergence of all quantities as we increase the bond dimension from 64 to 1024 in powers of 2. The observables are already nearly converged at $\chi = 64$. For example, the relative error in the condensate fraction between 64 and 1024 is below 1% for all but one (g, W) parameter point, and the relative error between 128 and 1024 is below 10^{-3} for all parameter points.

Also note one technical detail: on our actual device the interaction U is negative, and the experiment in fact is intended to adiabatically prepare not the lowest but the highest energy state within a fixed particle number sector. We therefore run DMRG on $-H$ rather than H , and we find the highest-excited state in the sector with unit filling.

Ideal adiabatic state preparation: In the experiment, we do not directly prepare the ground state but rather try to reach it using adiabatic state preparation. We also use MPS simulations, with the two-site time-dependent variational principle (TDVP) algorithm [67, 68], to simulate how the ideal Bose-Hubbard model behaves with the adiabatic ramps and 3 of the disorder realizations used in the experiment. (Because the ramp does not prepare an exact eigenstate, and hence the state continues to evolve during the hold time, we average the properties over the hold window, between $t = 105$ and $t = 115$ ns for t defined as shown in Fig. S7.)

All time evolution simulations are performed with a maximum bond dimension of 128; in the ground state search this was sufficient to converge all measured quantities to sufficient accuracy for comparison with the experiment. Here there is slightly higher entanglement due to the wavefunction including components of excited states, but even so the values of observables are almost indistinguishable comparing simulations with $\chi = 64$ and with $\chi = 128$. In particular the error is smaller than the typical errors in the experiment, so larger bond dimension are not necessary.

Effect of ramp-down after ideal adiabatic state preparation: One additional effect in the experiment that has not yet been taken into account is the necessity of including a ramp-down as the coupling strength must be brought back to 0 for readout. Ideally this would be an instantaneous quench, as shown in Fig. S7, in which case the wavefunction would not change before the measurement. However, for the physical device, a perfect quench is not possible. The true minimum ramp-down time is determined by details of the experimental hardware. For comparison with the experimental results, we simulate a linear ramp-down with two different durations: 1 ns and 3 ns.

Ground state of effective device Hamiltonian: As discussed in Sec. III, the physical quantum chip includes longer-ranged couplings, 3-body terms, and more that go beyond the idealized Bose-Hubbard model. To check what effect these couplings have on the quantities measured in the experiment, we perform direct ground state search with DMRG on the effective model from Schrieffer-Wolff perturbation theory, for comparison with the ground state results in the ideal Bose-Hubbard model. We simulate 10 disorder configurations from the experiment.

We organize the terms in the effective models by two size metrics. First, we consider the Manhattan distance (MD) between the farthest-separated sites acted on by operators in the term. For example, a term like $a_1^\dagger n_2 a_3$ acting on three qubits in a line would have MD=2. We also sort terms into 1-body (e.g. $a^\dagger a$), 2-body (e.g. $n_1 n_2$), 3-body, etc. Keeping all terms up to MD=3, 3-body, and coefficient larger than 1 kHz, for the largest couplings J we have more than 17000 terms on 36 sites, which we compress (almost losslessly) using deparallelization and delinearization [69] into a matrix product operator (MPO) of bond dimension around 150.

We investigate the convergence of observables with the number of terms kept, and we find that keeping terms up to MD=2 and up to 2-body gives results indistinguishable at the scale of experimental accuracy from keeping terms up to MD=3 and up to 3-body. Nevertheless, we use the full effective model in our DMRG data shown below.

Excited state calculations with MPS: To theoretically estimate the energies of the various phonon modes, we employ the MTDMRG method [70]. We obtain 35 excited states of the Bose-Hubbard model for the case of zero disorder, $W = 0$. The states computed using this method yield $\text{var}(\hat{H}) \sim 10^{-4}$ and the collective bundled (“multi-target”) MPS has $\chi = 3912$. To identify the states that we excite in the experiment, we examine the state that maximizes the overlap with the respective cosine profiles for each k_x mode, i.e.: $\text{argmax}_k (\sum_{l_x, l_y} \langle \psi_0 | \hat{n}_{l_x, l_y} | \psi_k \rangle \cos(k_x l_x))$.

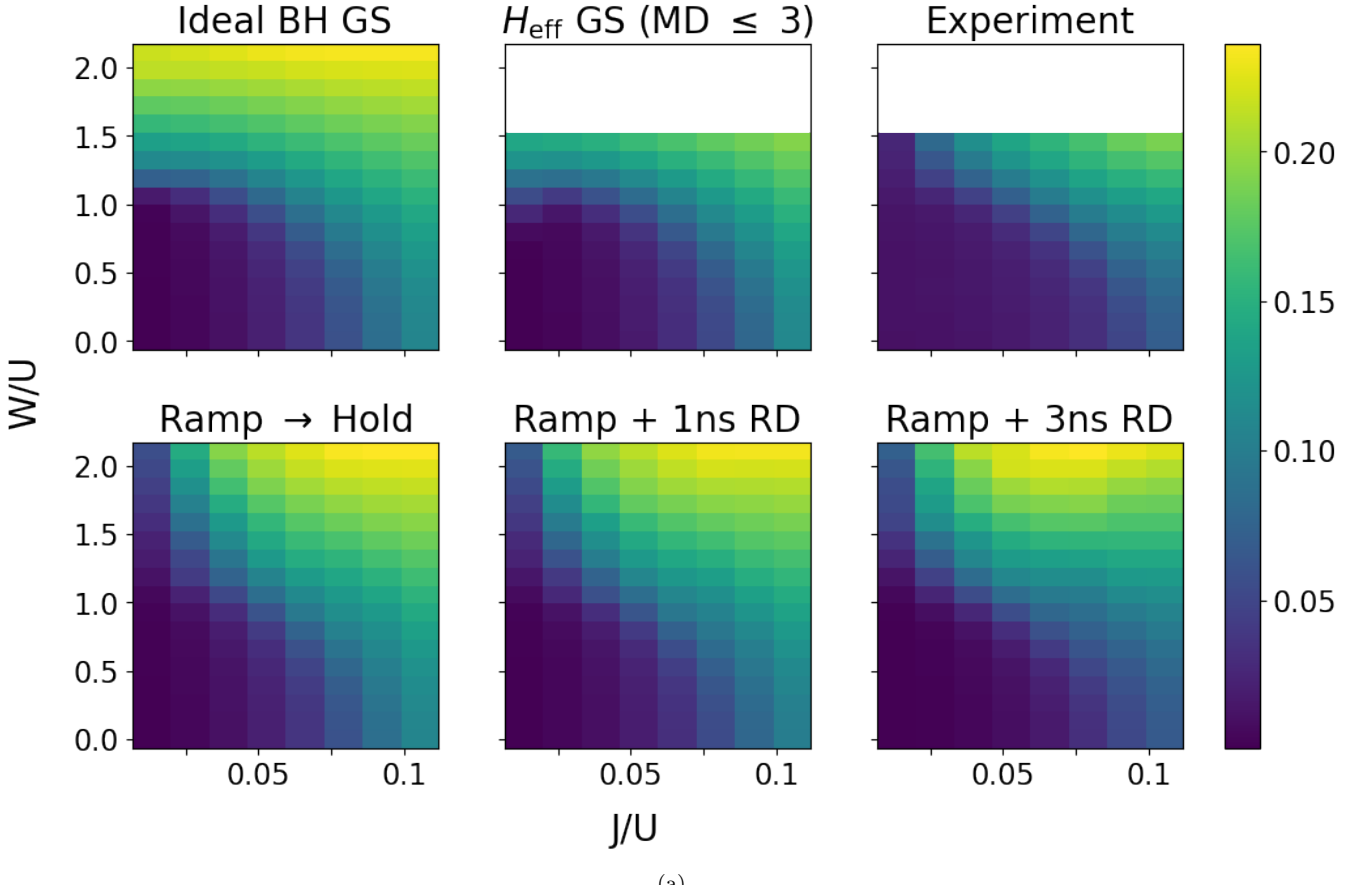
B. Results for various observables

Using each of these approaches to simulation, we compute observables from the wavefunctions in order to determine the phase diagram and compare with the experimental data. Here we focus on five quantities: doublon fraction, condensate fraction, entanglement entropy, inverse participation ratio, and compressibility.

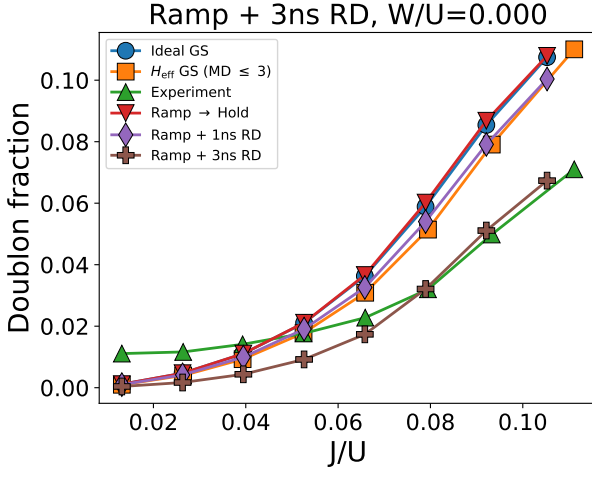
Doublon fraction: Specifically, we find $\langle a_i^{\dagger 2} a_i^2 \rangle / 2 = \langle n_i^2 - n_i \rangle / 2$. The $|0\rangle$ and $|1\rangle$ states do not contribute, so when truncating the local Hilbert space after the $|2\rangle$ state in the simulations, this quantity is precisely the probability of finding the system in $|2\rangle$ on site i . The result is shown in the full J - W parameter space in Fig. S8(a), and on cuts at $W = 0$ and $W/(2\pi) = 200$ MHz in Fig. S8(b) and (c). The figures include the experimental results (main text, Fig. 2) for easy comparison.

For the fixed- W cuts, we shift the plotted J values for the lines for the effective device Hamiltonian and for the experiment. When requesting a certain coupling strength on the device (as shown in the idealized experimental trajectory, Fig. S7, right panel), in the effective model from Schrieffer-Wolff perturbation theory we find that both J and U values are modified. Calling the new values J_{sw} and U_{sw} , we plot using $J_{\text{sw}}/U_{\text{sw}}$ in place of $J_{\text{ideal}}/U_{\text{ideal}}$.

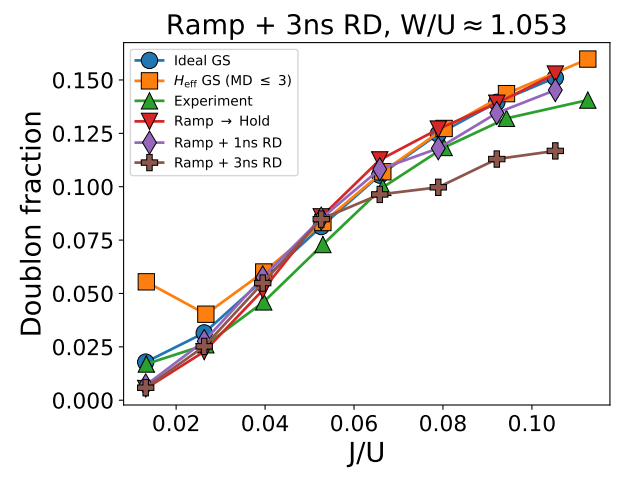
Also note that the simulations go to larger disorder strengths than used in the experiment, in order to give a more complete picture of the phase diagram.



(a)



(b)



(c)

FIG. S8. Doublon fraction. We compare the doublon fraction found in our experiment (main text, Fig. 2, reproduced here) with that found in each of a variety of MPS simulations described in Sec. IX A in the Supplement, including ground state search for the ideal Bose Hubbard model and the effective device Hamiltonian, as well as adiabatic state preparation with or without a ramp-down before measurement. Results from simulation are averaged over disorder instances taken directly from the experiment (10 for ground state simulations, 3 for time evolution simulations). Bond dimensions are up to 1024 for the ideal BH model ground state, and up to 128 for all other simulations; this is sufficient to converge all observables to the level visible in the figures. In (a) we show the results throughout parameter space, giving a qualitative picture of the extents of different phases and the rough scale of the observables. For a more quantitative picture, in (b) and (c) we show the values as a function of coupling strength J along two horizontal cuts with fixed disorder, $W/(2\pi) = 0$ and 200 MHz, respectively. In the latter figures, the J/U values for both the effective device model and the experimental data are shifted to the value derived in the effective model, rather than using the bare input J/U value.

Condensate fraction: We compute in the MPS all expectation values $\langle a_i^\dagger a_j \rangle$, and then take the largest eigenvalue of the corresponding single-particle density matrix. The result is shown alongside the experimental data in the full J - W parameter space in Fig. S9(a), and on cuts at $W = 0$ and $W/(2\pi) = 200$ MHz in Fig. S9(b) and (c). We also include the experimental data (shown in the main text in Fig. 4).

Entanglement entropy: We compute the entanglement entropy between left and right halves of the system. Highly localized phases like the Mott insulator have low entanglement, while the superfluid phase is highly entangled. The result is shown in the full J - W parameter space in Fig. S10(a), and on cuts at $W = 0$ and $W/(2\pi) = 200$ MHz in Fig. S10(b) and (c). Entanglement is not measured in the experiment.

Inverse participation ratio: The inverse participation ratio (IPR), $\sum_i |\psi_i|^4$ where $|\psi\rangle = \sum_i \psi_i |b_i\rangle$ summed over all computational basis bitstrings b_i . This is computed directly from the MPS with a cost $\mathcal{O}(\chi^5)$ where χ is the MPS bond dimension. A high value indicates a high degree of localization, corresponding to insulating and glassy phases. The results are shown in the full J - W parameter space in Fig. S11(a), and on cuts at $W = 0$ and $W/(2\pi) = 200$ MHz in Fig. S11(b) and (c). Note that we use a log scale because the IPR varies over about 7 orders of magnitude in the parameter space we consider.

Compressibility: Finally, we compute and plot compressibility. Results are shown in Fig. S12. Specifically, as in the experiment, in the simulations we apply a “tilt” to the system via a gradient in chemical potential along the long (9-site) direction and then measure the response in the local occupations $\langle n_i \rangle$. Compressibility cannot meaningfully be computed from the ground state throughout much of the phase diagram, since in the ground state with large tilt and only moderate disorder, it is often favorable to put doublons on the sites with lower chemical potential and holons on the sites with higher chemical potential, even as the coupling J goes to 0; the system then artificially appears compressible when in fact that state could not have been reasonable reached by an adiabatic procedure starting from uniform filling.

We therefore compare the experimental results (main text, Fig. 3) only with the results of the simulation of adiabatic state preparation plus a short (1 ns) ramp-down. There are two different procedures for the adiabatic preparation. In the “field-cooled” (FC) case, we first ramp the qubit frequencies to their tilted configuration, then ramp on the coupling, so that the system is “cooled” to the ground state through the adiabatic ramp with the tilt in chemical potential (the “field”) already applied. In the “zero-field-cooled” (ZFC) case, we turn on the couplings first, and only then add the tilt.

Especially in the FC case, we see that the simulation results actually look noisier than the experimental data. This is primarily due to the fact that we use just 5 disorder realizations in the simulations, compared with 150 in the experiment. All the other observables discussed above have only small variations in value between disorder realizations, whereas the compressibility varies widely.

Inverse participation ratio: The inverse participation ratio (IPR), $\sum_i |\psi_i|^4$ where $|\psi\rangle = \sum_i \psi_i |b_i\rangle$ summed over all computational basis bitstrings b_i . This is computed directly from the MPS with a cost $\mathcal{O}(\chi^5)$ where χ is the MPS bond dimension. A high value indicates a high degree of localization, corresponding to insulating and glassy phases. The results are shown in the full J - W parameter space in Fig. S11(a), and on cuts at $W = 0$ and $W/(2\pi) = 200$ MHz in Fig. S11(b) and (c). Note that we use a log scale because the IPR varies over about 7 orders of magnitude in the parameter space we consider.

C. Insights from comparison between experiment and simulation

Comparing the ground state of the ideal model with the experimental data, the phase diagram implied by the observables is qualitatively similar: the Mott insulator at small J and W is characterized by small doublon and condensate fractions, as well as low entanglement and a large inverse participation ratio, indicating that the state is nearly a product. At large J there is the superfluid phase characterized by large condensate fraction and high compressibility, and at intermediate J and large W there is the Bose Glass phase, which has doublons and no condensate.

However, there are some significant discrepancies. Of particular note, at small J and large W , we find a large density of doublons in the true ground state, which is not seen in the adiabatically prepared state in the experiment. Furthermore, the peak condensate fraction in the experiment is reduced by approximately a factor of 2 relative to the ground state, and the peak in the condensate fraction occurs at lower values of W in the experiment.

One possible source of these effects is that the ramp-up in the experiment is not sufficiently adiabatic to prepare the ground state. Comparing the “Ideal BH GS” and “Ramp \rightarrow Hold” panels in Figs. S8, S9, S10, and S11, we see that the ramp procedure does in fact explain the lower doublon count seen in experiment at low J and large W . When directly finding the ground state, when $W > 2U$, there will be some sites for which the energy gap (setting inter-site coupling to 0) between $|1\rangle$ and $|2\rangle$ is smaller than the average gap between $|0\rangle$ and $|1\rangle$ across all sites, so

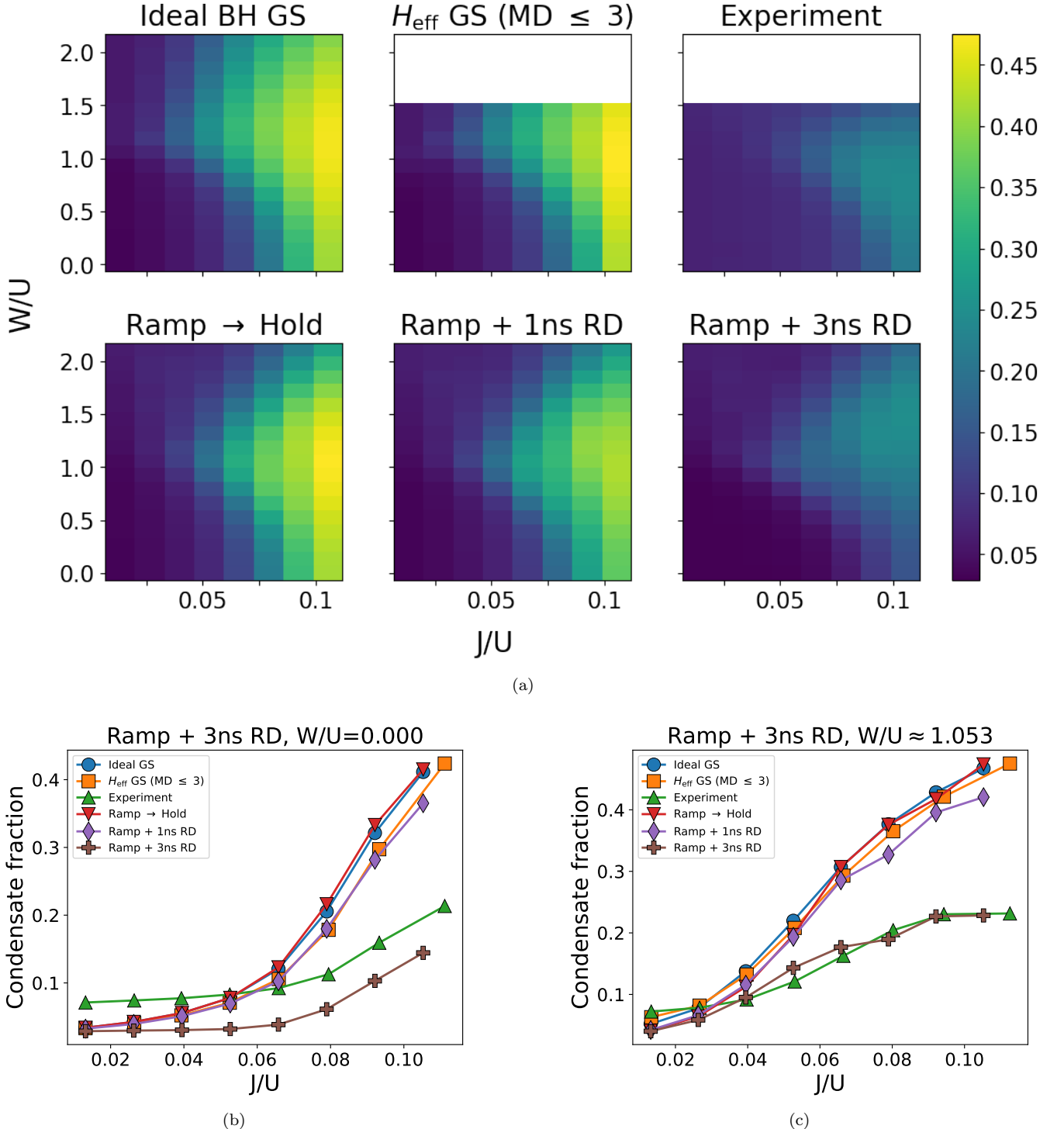


FIG. S9. **Condensate fraction.** We compare the condensate fraction found in our experiment (main text, Fig. 4, reproduced here) with that found in each of our variety of MPS simulations described in Sec. IX A. Disorder instances and bond dimensions are the same as in the previous figure. (a) Results throughout J - W parameter space. (b) and (c): Results for $W/(2\pi) = 0$ and 200 MHz, respectively.

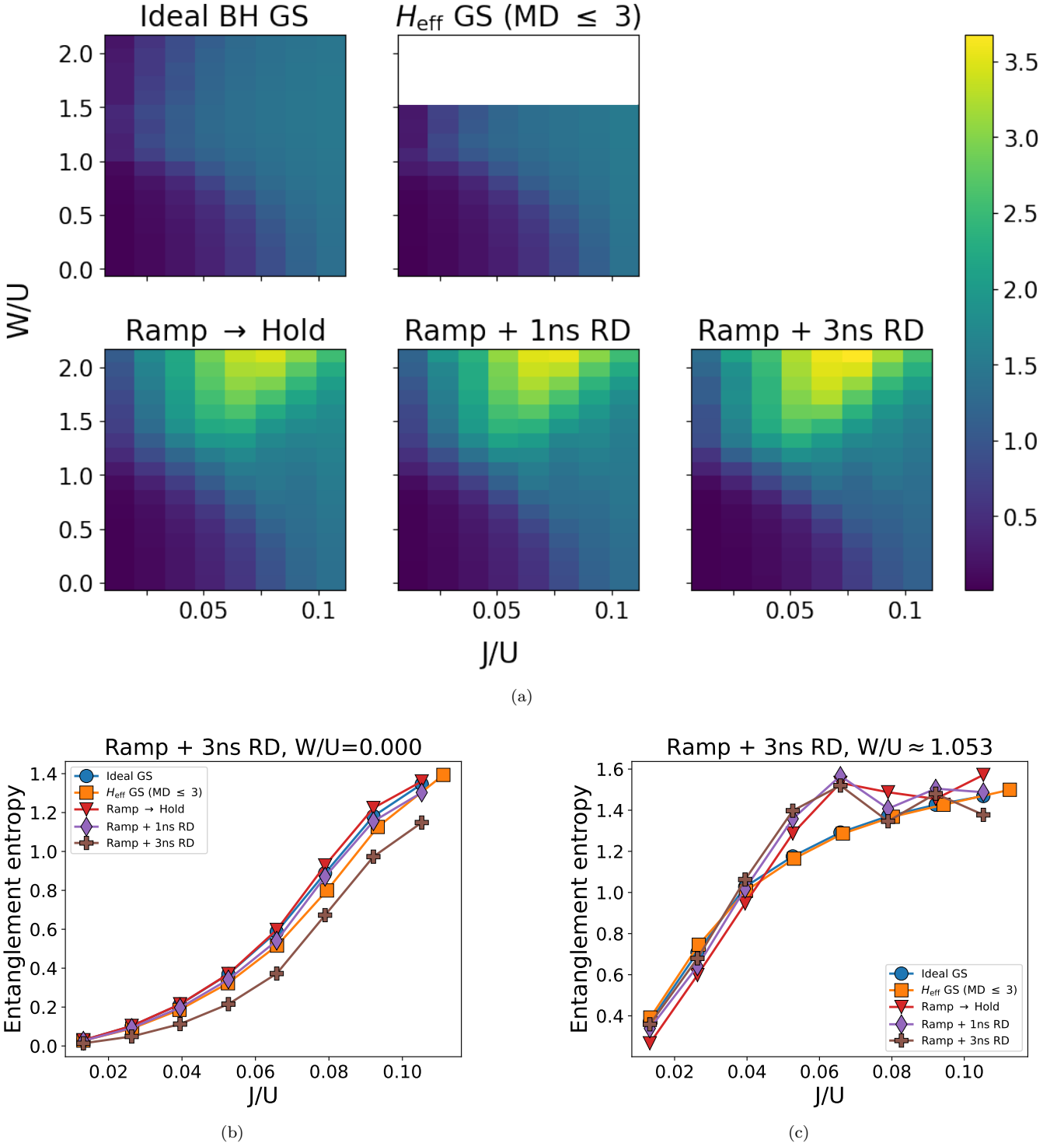


FIG. S10. **Entanglement entropy.** We compute the entanglement entropy in each of our variety of MPS simulations described in Sec. IX A. Disorder instances and bond dimensions are the same as in the previous figure. (a) Results throughout J - W parameter space. (b) and (c): Results for $W/(2\pi) = 0$ and 200 MHz, respectively. The entanglement clearly shows that, especially for intermediate coupling and large disorder, the ramp procedure produces a different state from the ground state of the Bose Hubbard model.

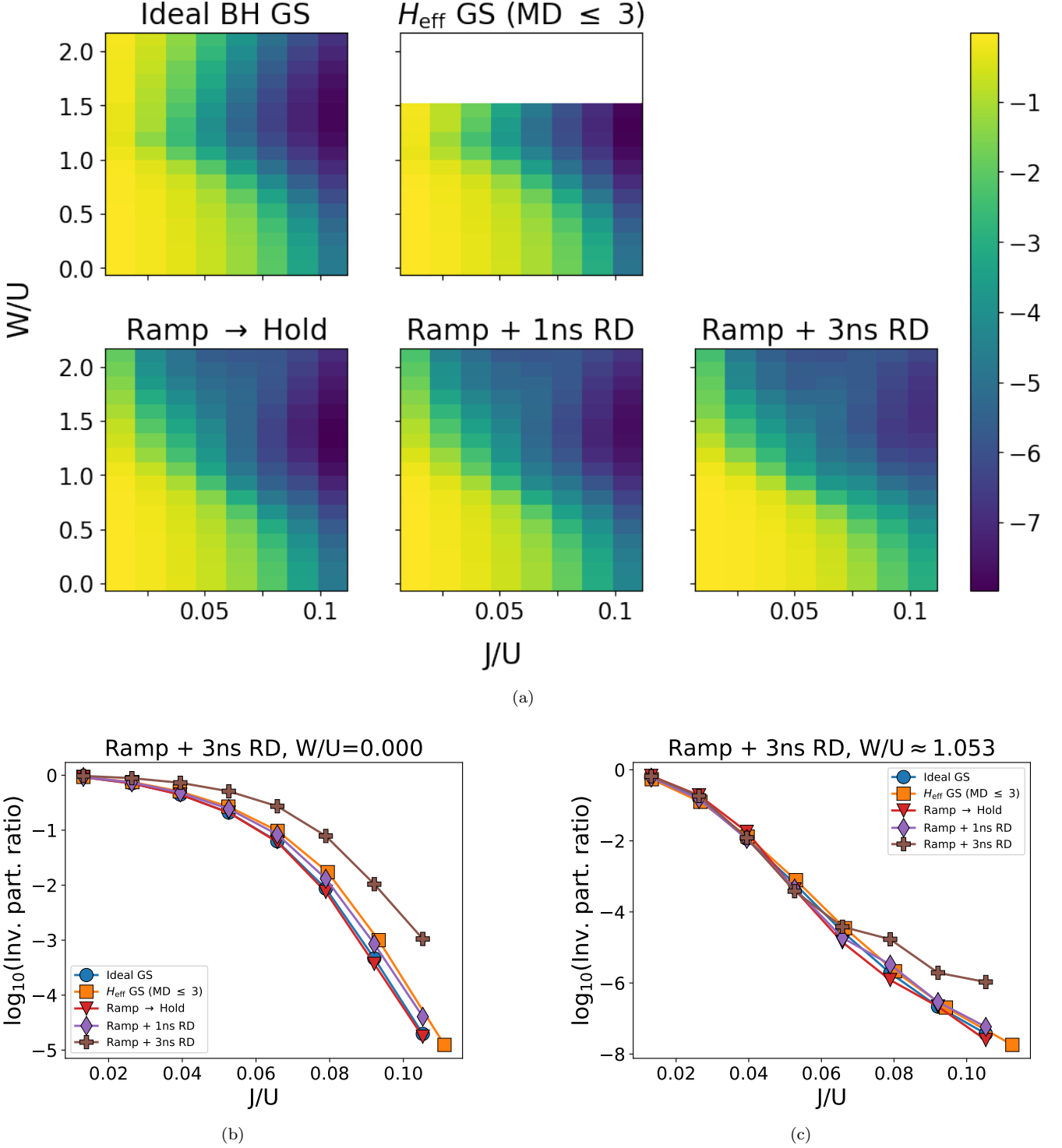


FIG. S11. **Inverse participation ratio.** We compute the inverse participation ratio (IPR) in each of our variety of MPS simulations described in Sec. IX A; the IPR is computed directly from the wavefunction, not via sampling. Because the value varies over several seven orders of magnitude across the parameter regime we consider, we plot $\log_{10}(\text{IPR})$. Disorder instances and bond dimensions are the same as in the previous figures. (a) Results throughout J - W parameter space. (b) and (c): Results for $W/(2\pi) = 0$ and 200 MHz, respectively. Like the entanglement entropy, the IPR shows that the ramp procedure prepares a state quite different from the ground state at intermediate J and large W .

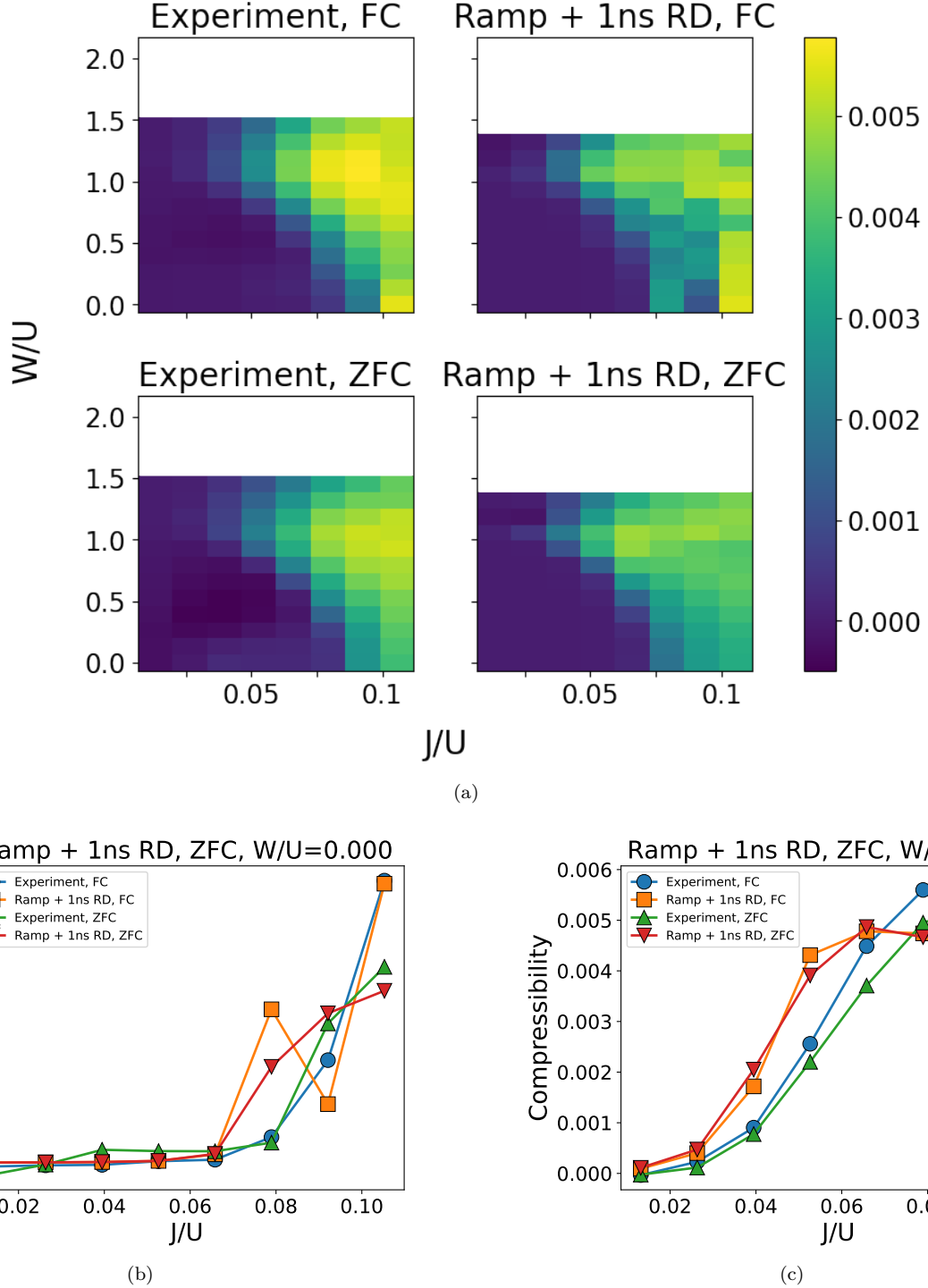


FIG. S12. **Compressibility.** We run MPS time evolution simulations to emulate the compressibility experiments (Fig. 3 in the main text). The setup and computation are exactly as for the experiment, except that the experiment uses 150 disorder realizations and the simulation uses only 5. Dynamics simulations are performed at bond dimension 128. (a) Results throughout J - W parameter space. (b) and (c): Results for $W/(2\pi) = 0$ and 200 MHz, respectively.

that a substantial number of doublons are expected due purely to on-site terms. On the other hand, these states are dynamically inaccessible with small coupling strength and the ramp times used in our experiment (and hence in the simulations of the adiabatic procedure).

The simulated adiabatic procedure still disagrees with the experiment on the magnitude of the condensate fraction

in the superfluid phase, as well as on the extent of that phase in parameter space. Adding a 1 ns ramp-down in the simulation has no significant effect on any measured observable. On the other hand, adding a 3 ns ramp-down, which is probably more accurate for the real device, does bring the magnitude of the condensate fraction much closer to what is seen experimentally, suggesting that the discrepancy from the true ground state may be due to the need to non-instantaneously turn off coupling before measurement.

Finally, we can ask whether long-ranged and many-body terms in the true device Hamiltonian also provide a possible explanation for the deviation of the experiment from the ideal ground state. However, as seen in the data, we find that none of the observables we consider are strongly impacted by these extra terms; the difference between observables in the ground state of the ideal model and the ground state in the effective device model is much smaller than the difference with the experimentally measured values.